CrossMark

SCUBA-2 Ultra Deep Imaging EAO Survey (STUDIES): Faint-end Counts at 450 μm

Wei-Hao Wang[1] , Wei-Ching Lin[1,2], Chen-Fatt Lim[1,3], Ian Smail[4] , Scott C. Chapman[5], Xian Zhong Zheng[6], Hyunjin Shim[7], Tadayuki Kodama[8] , Omar Almaini[9], Yiping Ao[6,8] , Andrew W. Blain[10] , Nathan Bourne[11], Andrew J. Bunker[12,13], Yu-Yen Chang[1], Dani C.-Y. Chao[14,35], Chian-Chou Chen[15,36] , David L. Clements[16] , Christopher J. Conselice[9] , William I. Cowley[17], Helmut Dannerbauer[18,19], James S. Dunlop[11], James E. Geach[20], Tomotsugu Goto[14], Linhua Jiang[21] , Rob J. Ivison[11,15] , Woong-Seob Jeong[22,23] , Kotaro Kohno[24,25] , Xu Kong[26], Chien-Hsu Lee[27], Hyung Mok Lee[28], Minju Lee[8,29] , Michał J. Michałowski[30], Iván Oteo[11,15] , Marcin Sawicki[31], Douglas Scott[32] , Xin Wen Shu[33] , James M. Simpson[1,37] , Wei-Leong Tee[1,2], Yoshiki Toba[1], Elisabetta Valiante[34], Jun-Xian Wang[26] , Ran Wang[21], and Julie L. Wardlow[4]

[1] Academia Sinica Institute of Astronomy and Astrophysics (ASIAA), No. 1, Section 4, Roosevelt Rd., Taipei 10617, Taiwan; whwang@asiaa.sinica.edu.tw
[2] Institute of Physics, National Taiwan University, Taipei 10617, Taiwan
[3] Institute of Astrophysics, National Taiwan University, Taipei 10617, Taiwan
[4] Centre for Extragalactic Astronomy, Department of Physics, Durham University, Durham DH1 3LE, UK
[5] Department of Physics and Atmospheric Science, Dalhousie University, Halifax, NS B3H 3J5 Canada
[6] Purple Mountain Observatory, Chinese Academy of Sciences, Nanjing 210008, China
[7] Department of Science Education, Kyungpook National University, Bukgu, Daegu 41566, Korea
[8] National Astronomical Observatory of Japan (NAOJ), Mitaka, Tokyo 181-8588, Japan
[9] School of Physics and Astronomy, University of Nottingham, Nottingham NG7 2RD, UK
[10] Department of Physics and Astronomy, University of Leicester, Leicester LE1 7RH, UK
[11] Institute for Astronomy, University of Edinburgh, Royal Observatory, Edinburgh EH9 3HJ, UK
[12] Department of Physics, University of Oxford, Oxford OX13RH, UK
[13] Kavli Institute for the Physics and Mathematics of the Universe, Kashiwa, 277-8583, Japan
[14] Institute of Astronomy, National Tsing Hua University, Hsinchu 30013, Taiwan
[15] European Southern Observatory, Garching, Germany
[16] Astrophysics Group, Imperial College London, Blackett Laboratory, London SW7 2AZ, UK
[17] Kapteyn Astronomical Institute, University of Groningen, Groningen, The Netherlands
[18] Instituto de Astrofísica de Canarias (IAC), Tenerife, Spain
[19] Universidad de La Laguna, Dpto. Astroísica, Tenerife, Spain
[20] Centre for Astrophysics Research, School of Physics, Astronomy and Mathematics, University of Hertfordshire, Hatield AL10 9AB, UK
[21] Kavli Institute for Astronomy and Astrophysics, Peking University, Beijing 100871, China
[22] Korea Astronomy and Space Science Institute, Yuseong-gu, Daejeon 34055, Korea
[23] University of Science and Technology, Yuseong-gu, Daejeon 34113, Korea
[24] Institute of Astronomy, University of Tokyo, Mitaka, Tokyo 181-0015, Japan
[25] Research Center for the Early Universe, University of Tokyo, Bunkyo, Tokyo 113-0033, Japan
[26] Department of Astronomy, University of Science and Technology of China, Hefei, Anhui 230026, China
[27] Subaru Telescope, NAOJ, Hilo, HI 96720, USA
[28] Department of Physics and Astronomy, Seoul National University, Seoul 08826, Korea
[29] Department of Astronomy, Graduate School of Science, The University of Tokyo, Bunkyo, Tokyo 113-0033, Japan
[30] Astronomical Observatory Institute, Faculty of Physics, Adam Mickiewicz University, 60-286 Poznań, Poland
[31] Department of Astronomy & Physics, Saint Mary's University, Halifax, B3J 3Z4, Canada
[32] Department of Physics and Astronomy, University of British Columbia, Vancouver, BC V6T 1Z1, Canada
[33] Department of Physics, Anhui Normal University, Wuhu, Anhui, 241000, China
[34] School of Physics and Astronomy, Cardiff University, Cardiff CF24 3AA, UK

Abstract

The SCUBA-2 Ultra Deep Imaging EAO Survey (STUDIES) is a three-year JCMT Large Program aiming to reach the 450 μm confusion limit in the COSMOS-CANDELS region to study a representative sample of the high-redshift far-infrared galaxy population that gives rise to the bulk of the far-infrared background. We present the first-year data from STUDIES. We reached a 450 μm noise level of 0.91 mJy for point sources at the map center, covered an area of 151 arcmin^2, and detected 98 and 141 sources at 4.0σ and 3.5σ, respectively. Our derived counts are best constrained in the 3.5–25 mJy regime using directly detected sources. Below the detection limits, our fluctuation analysis further constrains the slope of the counts down to 1 mJy. The resulting counts at 1–25 mJy are consistent with a power law having a slope of -2.59 (± 0.10 for 3.5–25 mJy, and $^{+0.4}_{-0.7}$ for 1–3.5 mJy). There is no evidence of a faint-end termination or turnover of the counts in this flux density range. Our counts are also consistent with previous

---

[35] Current address: Max Planck Institute for Astrophysics, D-85740 Garching, Germany
[36] ESO Fellow
[37] EACOA Fellow

SCUBA-2 blank-field and lensing-cluster surveys. The integrated surface brightness from our counts down to 1 mJy is $90.0 \pm 17.2 \, \mathrm{Jy \, deg^{-2}}$, which can account for up to $83^{+15}_{-16}\%$ of the *COBE* 450 μm background. We show that *Herschel* counts at 350 and 500 μm are significantly higher than our 450 μm counts, likely caused by its large beam and source clustering. High angular resolution instruments like SCUBA-2 at 450 μm are therefore highly beneficial for measuring the luminosity and spatial density of high-redshift dusty galaxies.

Key words: galaxies: high-redshift – galaxies: evolution – submillimeter: galaxies – cosmology: cosmic background radiation

1. Introduction

Since the advent of the Submillimeter Common User Bolometer Array (SCUBA; Holland et al. 1999) on the James Clerk Maxwell Telescope (JCMT) and the discovery of the first submillimeter galaxies (SMGs; Smail et al. 1997; Barger et al. 1998; Hughes et al. 1998; Eales et al. 1999) two decades ago, tremendous progress has been made in understanding this important dusty galaxy population (see reviews by Blain et al. 2002; Casey et al. 2014). Wide-field 850 μm surveys made with SCUBA and other bolometer array cameras have provided large samples of SMGs, while interferometric follow-up observations have enabled counterpart identification and detailed studies.

We now know that 850 μm-selected SMGs are ultraluminous ($L_{\mathrm{IR}} > 10^{12} \, L_\odot$) galaxies at $z \simeq 1$–6. Their redshift distribution peaks at $z \simeq 2.5$ (Chapman et al. 2003a, 2005; Barger et al. 2014; Simpson et al. 2014; Chen et al. 2016; Michałowski et al. 2017) with a $z > 4$ high-redshift tail (e.g., Wang et al. 2007; Younger et al. 2007; Dannerbauer et al. 2008; Asboth et al. 2016; Ivison et al. 2016; Shu et al. 2016). The exact redshift distribution of SMGs also strongly depends on the selection waveband; longer wavelengths may pick up SMGs at higher redshifts (e.g., Chapin et al. 2009; Roseboom et al. 2013; Zavala et al. 2014; Strandet et al. 2016). X-ray and infrared studies of 850 μm SMGs show that a modest fraction—about 20% of them—host active galactic nuclei, but most of them have total infrared luminosities dominated by star formation (Almaini et al. 2003; Alexander et al. 2005; Valiante et al. 2007; Pope et al. 2008; Menéndez-Delmestre et al. 2009; Laird et al. 2010; Wang et al. 2013). Their star formation rates (SFRs) are typically 10^2 to $>10^3 \, M_\odot \, \mathrm{yr^{-1}}$, and they contribute a significant fraction ($\simeq$30%) of the total SFR density at $z = 1$–5 (e.g., Barger et al. 2000, 2012; Chapman et al. 2005; Wang et al. 2006; Michałowski et al. 2010; Wardlow et al. 2011; Casey et al. 2013; Swinbank et al. 2014; Bourne et al. 2017; Cowie et al. 2017). On the other hand, it remains unclear whether the extremely large SFRs are triggered by major mergers or by disk instabilities. Results from multiwavelength morphological studies have not converged (Chapman et al. 2003b; Conselice et al. 2003; Swinbank et al. 2010, 2011; Chen et al. 2015; Simpson et al. 2015a; Hodge et al. 2016; Dunlop et al. 2017), and models that favor different mechanisms exist (Narayanan et al. 2010, 2015; Hayward et al. 2011, 2012; Lacey et al. 2016).

It is important to point out that attempts to understand the SMG population has been overwhelmingly focused on the bright end at 850 μm. The poor angular resolution of single-dish telescopes (e.g., FWHM = 15″ for JCMT at 850 μm) produces a relatively bright limit due to source blending ($S_{850} \sim 2$–3 mJy). This effect is known as "confusion" (Condon 1974); it prevents the detection of faint sources and the full resolution of the extragalactic background light (EBL). In the millimeter and submillimeter (mm/submm) bands, sources detected in single-dish confusion-limited blank-field surveys typically account for only 10%–40% of the EBL (Barger et al. 1999; Borys et al. 2003; Greve et al. 2004; Wang et al. 2004; Coppin et al. 2006; Weißet al. 2009; Scott et al. 2010; Hatsukade et al. 2011; Geach et al. 2017), and the bulk of the EBL remains unresolved. Surveys in strong lensing-cluster fields can nearly fully resolve the mm/submm EBL (Cowie et al. 2002; Smail et al. 2002; Knudsen et al. 2008; Johansson et al. 2011; Chen et al. 2013b; Hsu et al. 2016) and provide insight into the nature of the faint sources (Chen et al. 2014; Hsu et al. 2016). However, the sample sizes of such strongly lensed sources remain small, and source-plane expansion and magnification bias may make cosmic variance a stronger effect in lensing-cluster surveys.

Recently, ALMA has realized its tremendous sensitivity. Its high resolution makes it essentially confusion free and able to detect sources that comprise the bulk of the mm/submm EBL. However, because of the small primary beam of its antennas, unbiased ALMA surveys are only able to image a few arcmin^2 to substantial depths (Umehata et al. 2015; Aravena et al. 2016; Hatsukade et al. 2016; Dunlop et al. 2017). Larger samples of fainter sources, including those in the ALMA calibration fields (Oteo et al. 2016), have been serendipitously detected in ALMA archival data (Hatsukade et al. 2013; Ono et al. 2014; Carniani et al. 2015; Fujimoto et al. 2016), but biases caused by clustering and cosmic variance on these small scales are a potential concern.

The 450 μm window for deep submm surveys was truly opened up by SCUBA-2 (Holland et al. 1999). At 450 μm, the nearly two times increase in angular resolution from 850 μm makes SCUBA-2 much less confusion limited. This enables the direct detection of fainter SMGs. This also makes multi-wavelength counterpart identification less ambiguous. Previous 450 μm SCUBA-2 surveys reached sensitivities (1σ noise) of $\gtrsim$1 to 10 mJy in various blank fields and in lensing clusters. Among these, the deepest blank-field surveys (Geach et al. 2013; Zavala et al. 2017) resolved 20%–30% of the 450 μm EBL into point sources down to 6 mJy. Geach et al. (2013) also estimated that the confusion noise of JCMT/SCUBA-2 at 450 μm is approximately 1 mJy, but a detection limit of a comparable flux has not been reached by any blank-field surveys. On the other hand, lensing-cluster surveys (Chen et al. 2013a, 2013b; Hsu et al. 2016) reached intrinsic fluxes of $\sim$1 mJy on a smaller sample of highly magnified sources, and nearly fully resolved the EBL. For comparison, confusion-limited *Herschel* SPIRE imaging (FWHM $\simeq$30″ at 500 μm) can detect sources brighter than around 20 mJy at 250, 350, and 500 μm (Clements et al. 2010; Glenn et al. 2010; Oliver et al. 2010; Valiante et al. 2016), and these sources account for only about 15% of the far-infrared (FIR) EBL at these wavelengths. Unlike the 850 μm and millimeter bands, the 450 μm band has a weaker negative K-correction and is less sensitive to $z > 4$ galaxies, because the peak of the redshifted dust spectral energy distribution (SED) shifts out of the passband. However, for dust temperature of a few tens of

Kelvin, the 450 μm band probes the SED peak of galaxies at $z \simeq 1$–2, the peak epoch of both cosmic star formation and quasar activity. There is clearly great potential for SCUBA-2 to reach much deeper than *Herschel* at 450 μm and to detect the faint dusty galaxies that give rise to the bulk of the FIR EBL and hence the bulk of the cosmic star formation.

To exploit the potential of SCUBA-2, we initiated a new program, the SCUBA-2 Ultra Deep Imaging EAO (East Asian Observatory) Survey (STUDIES; program ID: M16AL006). It is one of the new JCMT Large Programs under the operation of EAO, starting from late 2015. Its goal is to map an $R \sim 8'$ region and get close to the confusion limit at 450 μm in three years with 330 hr of observations. The survey field is at the center of the Cosmic Evolution Survey (COSMOS; Scoville et al. 2007) within the area of the Cosmic Assembly Near-infrared Deep Extragalactic Legacy Survey (CANDELS; Grogin et al. 2011; Koekemoer et al. 2011). The STUDIES field is also within the wider and shallower SCUBA-2 survey of Casey et al. (2013). The southern shallower region of STUDIES overlaps with the 450 μm COSMOS pointing of the SCUBA-2 Cosmology Legacy Survey (S2CLS; Geach et al. 2013). STUDIES thus takes advantage of the extremely rich multiwavelength data in the COSMOS-CANDELS region and the heritage of previous SCUBA-2 surveys.

In its first year of observations, STUDIES accumulated approximately 40% of the data and reached an rms noise of 0.91 mJy at the map center at 450 μm. The image has a diameter of 15'. The full three-year STUDIES image will be 1.6× deeper over the same area. The parallel 850 μm imaging will provide an image that is confusion limited over the entire area. An early science result from STUDIES can be found in Simpson et al. (2017), where we detected a "passive" galaxy at 450 μm and demonstrated that non-detections in *Herschel* bands do not rule out an active star-forming system. Multiwavelength properties of the detected galaxies will be presented in our future papers. Because the progress in 2017 is much slower, caused by the poor weather and instrument servicing work, here we present the first-year STUDIES data and our improved constraints on the 450 μm source counts.

FIR and mm/submm number counts provide sensitive tests of galaxy evolution models (e.g., Baugh et al. 2005; Valiante et al. 2009; Béthermin et al. 2012b; Hayward et al. 2013; Cowley et al. 2015; Lacey et al. 2016; Béthermin et al. 2017) and require strong evolution in the properties of FIR luminous galaxies. The counts can also be compared with satellite EBL measurements to examine whether there remain significant galaxy populations that are unaccounted for in the imaging surveys. Ultimately, when the imaging surveys are sufficiently deep, the integrated surface brightness from the resolved source counts can put the various satellite EBL measurements to the test. We derive the 450 μm counts from both direct detections of bright sources and a fluctuation analysis for faint sources using the first-year STUDIES data. In Section 2, we describe the SCUBA-2 450 μm observations and data reduction. In Section 3, we derive the source counts at $S_{450} > 3.5$ mJy using direct 4σ detections and with simulations. We refer to this flux density regime as the "bright end." In Section 4, we examine the image background fluctuation below 4σ and use a maximum likelihood method (often referred to as "$P(D)$" analysis) to constrain the counts below 3.5 mJy. We refer to this as the "faint end." In Section 5, we compare our counts with other counts measurements and models, and estimate the

contributions to the 450 μm EBL. We summarize in Section 6. We analyze the various bias effects and source blending in our observations and source extraction in Appendix A, and verify that our results are not biased by source clustering at the scale of our beam size in Appendix B.

2. STUDIES 450 μm Data

2.1. Observations

We carried out the 450 μm SCUBA-2 observations between 2015 December 30 and 2016 May 11, under the best submm weather conditions on Maunakea (Band 1, $\tau_{225\,\text{GHz}} < 0.05$, or precipitable water vapor, PWV, <0.83 mm). SCUBA-2 also takes 850 μm data simultaneously, and the data will be presented elsewhere. The opacity was actively monitored with a water vapor radiometer using the 183 GHz water line at the telescope-pointing direction (Dempsey et al. 2012) to ensure that all observations were carried out under Band 1 conditions. The median PWV is 0.615 mm and the 90th percentile range is 0.440–0.803 mm, corresponding to 450 μm opacities of $\tau_{450\,\mu\text{m}} = 0.768$ and 0.590–0.958, respectively. Hourly telescope-pointing checks and less frequent focusing were conducted on the nearby infrared source IRC+10216. Typical pointing offsets were within 1″, much smaller than the 450 μm beam. Nightly flux calibration was obtained by imaging Uranus, Mars, and the infrared sources CRL 618, CRL 2688, and Arp 220. We conducted the imaging using the "CV Daisy" scan pattern,[38] which creates a circular map of $R \gtrsim 6'$ with an $R \simeq 1\rlap{.}'5$ deep core at the center and rapidly increasing noise at $R > 5'$. Each scan spanned 30 minutes in time. The scans were slightly offset from each other to even out the effects of noisy bolometers. This also slightly expands the map to $R \simeq 7\rlap{.}'5$. The total on-source time was approximately 120 hr, accounting for 40% of the total allocated integration of STUDIES.

2.2. Data Reduction

We performed the data reduction using the Sub-Millimeter Common User Reduction Facility (SMURF; Chapin et al. 2013) and the PIpeline for Combining and Analyzing Reduced Data (PICARD; Jenness et al. 2008). The time-stream data from the SCUBA-2 bolometers contain noise and signal from the background (atmosphere and ambient thermal emission), as well as astronomical objects. To extract the astronomical signal from the time streams and to map the results onto a celestial projection, we adopted the `Dynamic Iterative Map-Maker` (DIMM; Jenness et al. 2011; Chapin et al. 2013) routine of SMURF. We used the standard "blank-field" configuration file, which aims to detect extremely low signal-to-noise point sources from deep observations. First, flat fields were applied to the time streams using the flat scans that bracket each science observation. The flat-field procedure subtracts a polynomial baseline fit from each time stream and scales the data to units of pW. Next, DIMM enters an iterative stage that attempts to fit the data with a model comprising a common-mode background signal, astronomical signal, and noise. The iterations were repeated only four times, as we do not expect a single science scan to have any significant signal to well constrain the model. We verified that all of the final scans do not change significantly with further iterations,

---

[38] http://www.eaobservatory.org/jcmt/instrumentation/continuum/scuba-2/observing-modes/

meaning that the residual between the model and data has converged.

To obtain the absolute flux scale, we measured the flux conversion factors (FCFs) from a subset of 140 standard submm calibrators that were observed during the STUDIES campaign after excluding extreme values (usually from early evening and morning observations). We obtained a mean FCF of 490 Jy beam^{-1} pW^{-1} and an rms scatter of ± 136 Jy beam^{-1} pW^{-1}. The nominal value for SCUBA-2 at 450 μm is 491 ± 67 Jy pW^{-1} (Dempsey et al. 2013). Our scatter is twice larger than this and those in earlier SCUBA-2 450 μm studies in the literature. An about twice larger yearly scatter is also seen in the SCUBA-2 Calibration Database[39] for 2016. The large scatter in our FCF therefore indicates a real night-to-night variation rather than problems in our data or our reduction. However, other than the larger scatter, we do not observe a long-term trend in the mean FCF, and our mean FCF is consistent with the nominal value. We therefore applied the value of 490 Jy beam^{-1} pW^{-1} to our data. In general, we expect a 12% uncertainty in flux calibration (Dempsey et al. 2013), which is a combination of a 5% uncertainty in the absolute calibration of planetary models and another 10% uncertainty in the determination of the FCF.

After each scan was reduced and flux calibrated, we adopted the MOSAIC_JCMT_IMAGES recipe from PICARD to combine all of the products into a final map. To optimize the detection of point sources, we convolved the map with a Gaussian kernel that is matched to the instrumental point-spread function (PSF). For this, we adopted the PICARD recipe scuba2_matched_filter, which first smooths the map by convolving it with a 20″ Gaussian kernel and subtracts this smoothed map from the image to remove any large-scale structure. Then, a normalized Gaussian kernel with an FWHM set to the diffraction limit of the telescope was used to convolve the map to obtain the optimal point-source signal-to-noise ratio (S/N) for each pixel (Stetson 1987; Serjeant et al. 2003). The same process was also applied to the calibrators before the FCF was measured. Also, although the above procedure builds in a flux adjustment to compensate for the flux loss caused by the subtraction of the 20″ smoothed image, additional adjustment may be required. In order to see the effect on source fluxes of the blank-field configuration of DIMM and the above convolution procedures, we inserted artificial point sources with the instrumental FWHM into the data streams. For source flux densities from sub-Jy to a few Jy, we found that the above reduction procedures attenuated the flux density by 6.2%, on average. We therefore made a 6.2% flux adjustment to the map. This is slightly less than the 10% adjustment reported by Geach et al. (2013) and Chen et al. (2013b), but the difference is well within the generally accepted 10% calibration uncertainty.

Our final match-filtered map has a noise at the map center of 0.91 mJy for a point source, and the noise increases to around 10 mJy toward the map edge at a radius of 7′.5. The 0.91 mJy sensitivity is about 30% deeper than that in the deepest 450 μm map in the literature (Zavala et al. 2017) and is comparable to the deepest 450 μm pointing in S2CLS (J. E. Geach et al. 2017, in preparation). We present our S/N map in Figure 1 and the histograms of the pixel flux in Figure 2. In Figure 1, we can see negative rings, produced by the above match-filtering process, around the brightest sources. Relative to pure noise, the negative ring in the
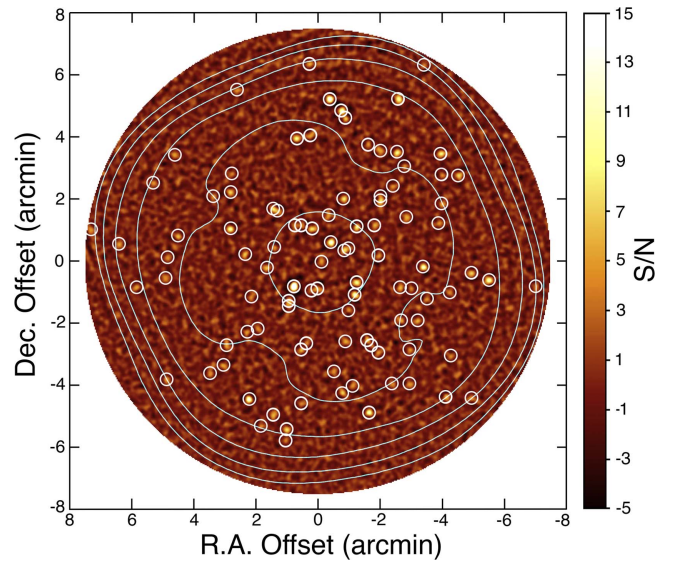

Figure 1. STUDIES 450 μm S/N map. Only the deeper $R = 7′.5$ is shown here. The map center is at R.A. = 10:00:30.2, decl. = +02:26:50. The contours represent noise levels from 1 mJy with a multiplicative step of $\sqrt{2}$. Sources detected at 4σ are marked with $R = 12″$ circles; there are 98 such sources. The easternmost source is not included in our number counts because of the requirement on noise of the source flux. Several of them have nearby companions with distances of $\sim 10″$, identified by our CLEAN-like source extraction algorithm (Section 3.1). There are an additional 43 sources detected at 3.5σ–4σ. These fainter sources are not labeled here to avoid confusion.
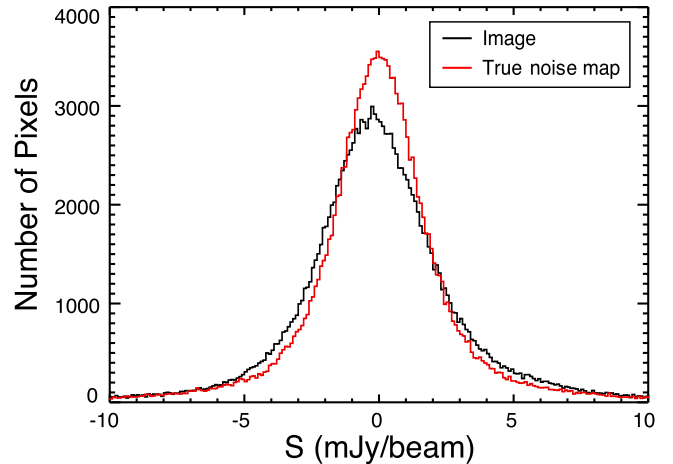

Figure 2. Distribution of pixel brightness in the 450 μm image (black) and in the "true noise" map (red; see Section 3.2). The excesses in the both positive and negative sides of the image are produced by celestial objects and the negative bowling in the PSF. The noise histogram is a sum of Gaussians of various widths, because of the non-uniform sensitivity distribution.

PSF is responsible for the negative excess in Figure 2. We verify the astrometry of our image by comparing the source positions in our image and in the Very Large Array 3 GHz image (Smolčić et al. 2017). Among the 98 4σ sources extracted from our image (Section 3.1), 59 have 3 GHz counterparts with 4″ search radii. We expect 1.3 of them to be chance alignments, given the spatial density of the radio sources. The mean positional offset between 450 μm and 3 GHz is 0″.3 along R.A. and 0″.2 along decl., and the dispersions are $\sim 1″.5$. These are all much smaller than the 450 μm beam. There is thus not an apparent astrometric offset in our image.

3. Source Detection and Number Counts

3.1. Source Extraction

We first constructed a PSF for source extraction. We generated a synthetic PSF by averaging the 10 highest S/N sources in our final match-filtered map. These 10 sources contribute equally to the averaged PSF. The resulting PSF has an FWHM of $10\rlap{.}''1$, which is 9% broader than an idealized PSF (i.e., instrumental PSF with the same matched filtering), likely caused by the minor smearing effects from pointing errors and focus changes. In the steps described below, we tried using the synthetic PSF and the idealized PSF. The results are in agreement with each other, except that the idealized PSF has a slight tendency to "detect" more faint sources very close to bright sources. This is likely caused by its narrower profile and the undersubtraction of the outer part of bright sources. Since the synthetic PSF contains the smearing effect from observations and should be more realistic, we adopt the synthetic PSF in the subsequent analyses.

To extract sources, we employ an iterative procedure that is similar to the "CLEAN" deconvolution in radio interferometric imaging (Högbom [1974](#)). We identify the peak pixel in the S/N map and subtract 5% of a peak-scaled synthetic PSF at its position. This 5% subtraction fraction is often called CLEAN "gain," and is typically set to a few to 10 percent in order to achieve stable convergence. We record its coordinates and subtracted flux. We identify the next peak in the image and repeat the process until we meet a floor S/N threshold, which we set to be 3.5σ. During the process, if a subsequent S/N peak is located within $4''$ (approximately half the beam FWHM) from a previously identified peak, we consider them to be the same source. In such a case, we only perform the iterative subtraction at the original position. Otherwise, we consider it to be a new source and perform the PSF subtraction at the new position. Since the cleaning of the source flux stops at 3.5σ, we sum up the cleaned fluxes and the remaining 3.5σ flux to be the final flux for each individual source. The very outer part of the map receives a much shorter integration and contains arc and stripe patterns that are clearly not random noise. Visual inspection shows that sources extracted in such areas are not always convincing. We therefore only include sources extracted within $7\rlap{.}'5$ (rms noise <10 mJy) from the map center in our final catalog. We detect 141 sources at 450 μm at $>3.5\sigma$, among which 98 are $>4.0\sigma$ (circles in Figure [1](#)).

The above iterative algorithm is inspired by the radio CLEAN deconvolution and is similar to that in Wang et al. ([2004](#)). It has the capability of separating mildly blended sources whose separation is larger than roughly one beam FWHM. For example, a pair of blended SCUBA sources in Wang et al. ([2004](#)) was subsequently confirmed by the interferometric imaging of Wang et al. ([2011](#)) to be multiple sources. In our 3.5σ and 4σ catalogs, there are seven and five pairs, respectively, whose separations are less than $12''$ (see Figure [1](#) for the 4σ cases). They will be targets of our future follow-up observations to test the accuracy of our source extraction in such limiting cases. We also note that when the CLEAN gain is set to 1.0, our source extraction reduces to the standard source identification adopted by other teams for SCUBA-2 images. The few close pairs would have been identified as single sources if the gain were 1.0. In our simulations (Appendix [A](#)), this would increase the fraction of sources that are blends of multiple faint sources (hereafter the "multiple fraction")
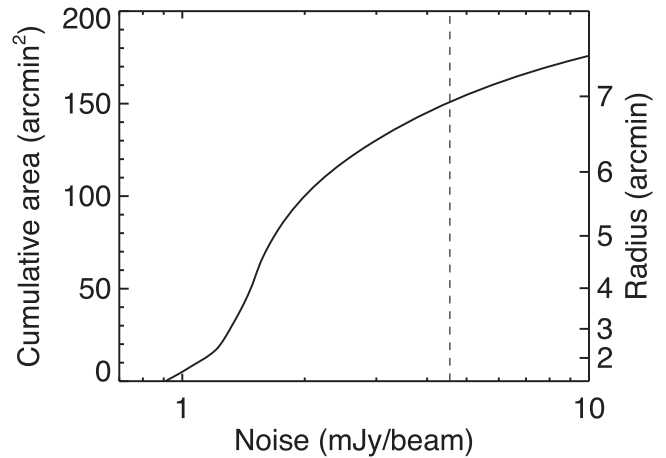

Figure 3. Cumulative map area vs. noise level. The noise distribution in our image is roughly axisymmetric, so the area can also be approximately mapped to the radius, which is shown on the right-hand y-axis. The map center has a noise of 0.91 mJy beam^{-1}. The noise slowly increases to $\sim$2 mJy beam^{-1}, where the map area reaches 100 arcmin^2. After that, the noise increases more rapidly toward the outer region. For our number counts, we do not use an image area that is more than five times shallower than at the map center, which is indicated by the vertical dashed line.

of the catalog. Also, in such a case, fluxes can be overestimated for blended sources, since their fluxes are contaminated by their neighbors. However, the previous SCUBA-2 450 μm surveys are shallower and farther from the confusion limit. Source blending and therefore the flux contamination may not be an issue there.

3.2. Number Counts and Simulations

We derived 450 μm source counts using our extracted sources and the noise map. We only use 4σ sources for this calculation because they are more secure detections. We will discuss the reliability of the 4σ sources in Appendix [A](#). Furthermore, to ensure reliable source counts on faint sources, we confine our calculations to areas where the noise is less than five times the noise of the map center. This further discards the noisiest 9% of the area used for the source extraction. The cumulative area as a function of noise is shown in Figure [3](#), and the area involved in our estimates is 151 arcmin^2, indicated by the vertical dashed line. Of the 98 4σ sources, 97 fall in this area.

In the number count calculation, each source contributes $1/(A_e(S)dS)$ to the counts, where A_e is the effective area where the source can be detected at $>4\sigma$ given its measured flux density S, and dS is the flux density interval. Essentially, $A_e(S)$ is the function in Figure [3](#) when the x-axis is multiplied by 4. The error is assumed to be Poissonian. The faintest flux density bin is discarded, because it only contains one source. The resulting raw differential counts are presented in Figure [4](#) (open squares) and Table [1](#) (column 3).

The raw counts suffer from various observational biases: flux boosting produced by the Eddington bias and faint confusing sources; detection incompleteness; spurious sources; and source blending. These are analyzed in detail in Appendix [A](#). To overcome these, we performed Monte Carlo simulations to derive the intrinsic counts. We first created a "true noise" map using the jackknife method, described by Cowie et al. ([2002](#)) for SCUBA imaging. We divided the half-hour SCUBA-2 scans into two interlacing halves and made two maps of nearly
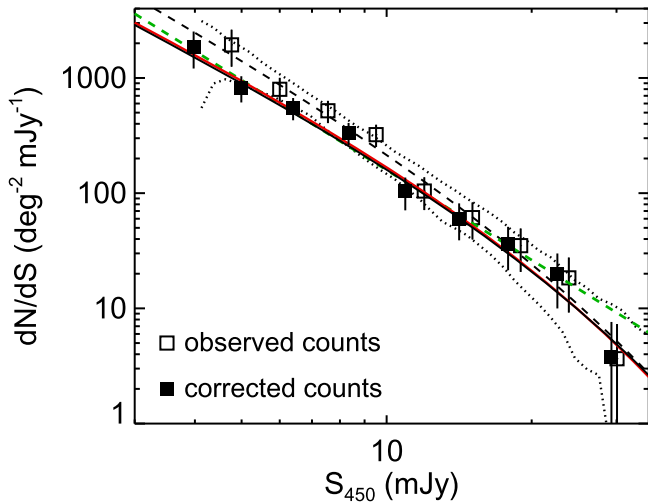
Figure 4. Differential 450 μm counts. Open squares are the observed raw counts and solid squares are the corrected counts. The raw and corrected counts have different fluxes because of the correction for flux boosting (Appendix A). The solid black curve is the input Schechter counts in the simulations. The dashed black curve is the measured output counts in the simulations and can also be described by a Schechter function. The two dotted black curves show the 68th percentile range of the outputs of the 200 realizations. The 68th percentile range reasonably matches the observed error bars derived based on the assumption of Poisson errors. Two parameterizations to the corrected counts are shown with colored curves. The red solid curve is a Schechter fit to the corrected counts. The reduced χ^2 of this fit is 0.45 ($N_{\rm df} = 6$). This curve is almost indistinguishable from the input Schechter function (black solid curve), showing that our iterative procedure converges. The green dashed line is a power-law fit to the corrected counts after excluding the brightest flux density bin. The reduced χ^2 of this fit is 0.38 ($N_{\rm df} = 6$).

identical area coverage and sensitivity. The two half-maps underwent the same beam-matched convolution as the full map. They were subtracted from one another, and each pixel of the resultant map was scaled by $\sqrt{t_1 t_2}/(t_1 + t_2)$, where t_1 and t_2 are the noise-weighted integration times of that pixel in the two half-maps. (t_1 and t_2 are not identical because a fixed sky position can be swept by different bolometers in different scans.) This effectively removes any faint sources and provides a map with noise distribution identical to the real image. We measured the rms noise locally on the true noise map and found it to be consistent with the rms map generated by SMURF. The brightness distribution in the true noise map is presented in Figure 2 (red histogram). It is symmetric about zero. It is Gaussian-like, but not exactly a Gaussian. Instead, it is a sum of Gaussians of various widths, because of the non-uniform sensitivity distribution,

We then created simulated images using the synthetic PSF. We randomly placed scaled PSFs in the true noise map with assumed source counts (see below) and flux densities between 1 and 50 mJy. We found that this 1–50 mJy flux density range is sufficient, and the results do not change if we expand the range for the input sources (see Section 4). In each fine flux density bin, the number of simulated sources is determined by the assumed counts plus a Poissonian fluctuation. We created 100 simulated images using each of the positive and negative true noise maps. Because all of the effects of flux boosting, completeness, spurious sources, and source blending depend on the intrinsic source counts, the selection of the intrinsic counts in the simulations may be crucial. We employed an iterative procedure to approach the intrinsic counts from the observed raw counts. We started with assuming that the intrinsic counts

are the observed raw counts; we fit the raw counts with a Schechter function and used the fitted function as input to create the first set of 200 realizations. We then ran source extraction on the simulated images, derived simulated output counts, and compared them with the observed raw counts. We calculated the ratio between the simulated and observed counts, used that to adjust the input counts, and repeated the simulations. In the first two iterations, the simulated output counts fluctuated around the observed counts and then converged after the third iteration. In the third iteration, the required adjustment was much smaller than the error bars in the counts. Our final corrected counts ($C_{\rm corr}$) are calculated using the raw counts ($C_{\rm raw}$) and the ratios between the input and output counts in the simulations ($C_{\rm sim,in}$ and $C_{\rm sim,out}$, respectively):

$$C_{\rm corr}(S_{\rm corr}) = C_{\rm raw}(S_{\rm obs}) \times \frac{C_{\rm sim,in}(S_{\rm corr})}{C_{\rm sim,out}(S_{\rm obs})}, \qquad (1)$$

where $S_{\rm obs}$ is the observed flux density of the sources and $S_{\rm corr}$ is the flux density corrected for boosting (see Appendix A). The corrected counts are presented in Table 1 (column 5) and in Figure 4 (solid squares). For the readers' reference, we also present the corrected cumulative counts in Table 1 (column 7), derived in the same manner as the differential counts.

Our calculation in Equation (1) is fundamentally different from what is often adopted in the literature for mm/submm single-dish source counts, where the counts are corrected with completeness and spurious fractions. For such corrections, one generally has to assume one-to-one relations between the input and output source lists. Such an assumption is not accurate for single-dish observations, because multiple sources in the input list can be blended in the image and detected as a single source of very different flux densities in the output list. In contrast, Equation (1) does not rely on such an assumption. The only part in Equation (1) that contains a one-to-one relation is the correction of the observed flux density ($S_{\rm obs}$) to intrinsic flux density ($S_{\rm corr}$), and this is presented in Appendix A. However, this only slightly affects the interpretation of where the counts are measured in terms of intrinsic flux density and does not change the measured amplitude and slope of the counts.

The corrected counts in Figure 4 can be fit reasonably well with a Schechter function,

$$\frac{dN}{dS} = \left(\frac{N_0}{S_0}\right)\exp\left(-\frac{S}{S_0}\right)\left(\frac{S}{S_0}\right)^\alpha \ {\rm deg}^{-2} \ {\rm mJy}^{-1}, \qquad (2)$$

with the best-fitting parameters listed in Table 2. The reduced χ^2 of the fit is 0.45, for a degree of freedom of $N_{\rm df} = 6$. The fitted function is the red solid curve in Figure 4. This fitting is considered as the final (fourth) iteration to approach the intrinsic counts. It is almost indistinguishable from the input Schechter function used to create the simulations (black solid curve in Figure 4), showing that the iteration converges very nicely. In the studies of Chen et al. (2013b) and Hsu et al. (2016), similar iterative procedures were also adopted, and the fitting of the intrinsic counts was made as part of the analysis procedure.

In the literature, mm/submm counts are also often fitted with a broken double power law. The turnover point is typically between 20 and 30 mJy for 450 μm counts (Casey et al. 2013; Chen et al. 2013a, 2013b; Hsu et al. 2016; Zavala et al. 2017),

Table 1
450 μm Counts

	Differential Counts				Cumulative Counts	
N	$S_{\rm obs}$ (mJy)	Raw dN/dS (deg^{-2} mJy^{-1})	$S_{\rm corr}$ (mJy)	Corrected dN/dS (deg^{-2} mJy^{-1})	$S_{\rm corr}$ (mJy)	Corrected $N(>S)$ (deg^{-2})
9	4.77	1938 ± 686	3.94	1906 ± 674	3.57	4662 ± 709
16	6.00	797 ± 204	5.02	814 ± 209	4.45	3132 ± 363
21	7.55	519 ± 113	6.45	538 ± 118	5.64	2252 ± 273
21	9.51	322 ± 70	8.36	331 ± 72	7.29	1419 ± 202
10	12.0	104 ± 33	10.9	105 ± 33	9.55	730 ± 136
8	15.1	61.4 ± 21.7	14.1	61.3 ± 21.7	12.5	447 ± 103
6	19.0	35.0 ± 14.3	17.9	35.8 ± 14.6	15.9	254 ± 76.7
4	23.9	18.4 ± 9.2	22.7	19.6 ± 9.8	20.0	119 ± 53.2
1	30.1	3.65 ± 3.65	29.0	3.97 ± 3.97	25.7	22.8 ± 22.8

Note. $S_{\rm obs}$ is the observed flux density. $S_{\rm corr}$ is the flux density corrected for boosting (Appendix A). For the differential counts, the flux densities are the center of the bins. For the cumulative counts, the flux densities are the lower ends of the bins.

Table 2
Parameterizations for the Corrected Counts

Parameter	Schechter Fit (Equation (2))	Power-law Fit (Equation (3))
N_0	2136 ± 189 deg^{-2}	62,400 ± 13,400 deg^{-2} mJy^{-1}
α	−2.02 ± 0.10	−2.59 ± 0.10
S_0	15.07 ± 0.79 mJy	...
χ^2	0.45	0.38
$N_{\rm df}$	6	6

Note. The fitting is conducted on the bright-end counts above 3 mJy. For the power-law fit, the brightest flux density bin is not included.

and 8.4 mJy for 850 μm counts constrained by ALMA (Simpson et al. 2015b). These two are consistent given that the S_{850}/S_{450} ratio is typically 2.5 with a large scatter (Casey et al. 2013; Hsu et al. 2016). Our data also seem to suggest a turnover point at 20–30 mJy, but we do not have sufficient data to constrain the slope in the brighter portion. If we fit our data with a broken power law, we get a turnover flux density between our first and second brightest flux density bin, and thus no constraint on the bright-end slope. This is essentially fitting the counts with a single power law after excluding the brightest flux density bin. We therefore fit our counts at $S < 25$ mJy with a power-law form,

$$\frac{dN}{dS} = N_0 \left(\frac{S}{\rm mJy}\right)^{\alpha} {\rm deg}^{-2}\,{\rm mJy}^{-1}, \qquad (3)$$

with the best-fitting parameters listed in Table 2. The reduced χ^2 of the fit is 0.38 ($N_{df} = 6$). This is the green dashed line in Figure 4 and is a slightly better fit to the data at <25 mJy, compared to the Schechter fit. If we exclude the brightest flux density bin and then perform a Schechter fit, we obtain a large S_0 (>60 mJy) and strong degeneracies among the fitted parameters. This again shows that the data at <25 mJy are consistent with a single power law.

4. Fluctuation Analyses for the Faint End

The derivation of the source counts in the previous section makes use of sources detected at 4σ at above 3.5 mJy (intrinsic). The flux distribution of the residual map after 4σ
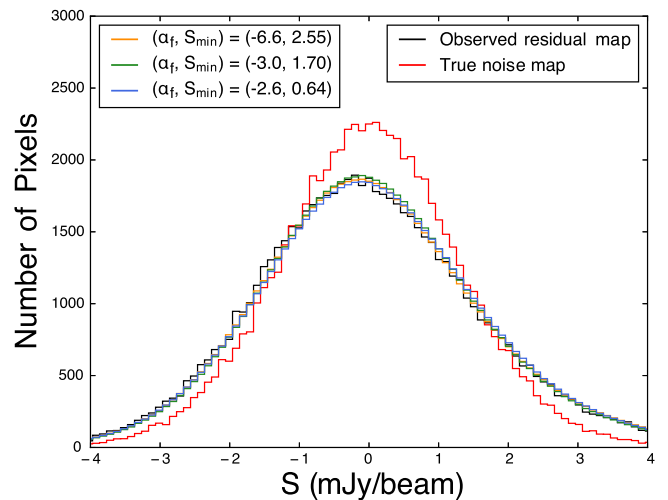

Figure 5. Distributions of pixel brightness in the residual maps from the observations (black), true noise map (red), and three representative models from our fluctuation analysis that have high likelihoods (orange, green, and blue, corresponding to the three crosses in Figure 6). Here we only show the pixels within 5′ of the map center, i.e., the pixels included in our fluctuation analysis.

sources are removed contains additional information about fainter sources. In Figure 5, we show the flux distribution of the pixels within 5′ of the map center in the residual map and in the true noise map. The noise level in this area is 0.91–1.5 mJy. Compared to pure noise fluctuations, the residual map has excesses on both the positive and negative sides, caused by <4σ faint sources and the negative rings around their PSF. This shape can be used to further constrain the faint-end counts. To do this, we employ a parameter estimation method similar to that described in Patanchon et al. (2009; see discussion therein). In the literature, Maloney et al. (2005), Coppin et al. (2006), Weißet al. (2009), and Scott et al. (2010) also used similar methods to derive counts from their mm/submm images. The idea is to minimize the difference in the flux density distributions of the model-predicted and the measured residual maps by maximizing the likelihood. In the literature, this is often referred to as the $P(D)$ method.

For each number count model, the likelihood of the data is the probability that all of the flux density values in the residual

map occurred, in logarithmic form:

$$\ln L(\theta) = \sum_k \ln(p(d_k|\theta)), \qquad (4)$$

where θ represents the generalized model parameters, $d = \{d_1,\ldots,d_k,\ldots\}$ is the set of flux density values of the pixels, and $p(d_k|\theta)$ is the probability distribution function (PDF) of individual flux values with respect to the model. Assuming that the PDF does not vary strongly in a flux density bin, we then have

$$\ln L(\theta) = \sum_i n_i \ln(p_i(\theta)), \qquad (5)$$

where n_i is the number of pixels in the ith flux density bin and $p_i(\theta)$ is the integral of the PDF in the ith bin. Equation (5) is what we adopt to calculate the log-likelihood for a number count model, and the PDF is equivalently the flux density histogram of the pixels in an image.

For simplicity, we adopt a single power law with only two parameters for the faint-end counts. The first one is the termination point of the counts, $S_{\min}$. The counts are assumed to be zero at $S < S_{\min}$, and $S_{\min}$ can be chosen to be much fainter than the detected sources. The second parameter is the faint-end power-law slope, denoted as α_f. The power law is normalized to the corrected bright-end count at 3.94 mJy. This is the median flux density in the faintest flux density bin of our corrected bright-end counts. In principle, we could add a third parameter so that the junction point of the bright and faint ends does not have to be 3.94 mJy. Furthermore, we should allow a faint-end turnover at perhaps below 1 mJy in order to prevent the sources from overproducing the EBL; this would require two additional parameters (the turnover flux density and the slope in the extreme faint end). However, as we will show, the results of the two-parameter model are already highly degenerate, and our data do not allow meaningful constraints on additional parameters.

To determine the PDF of each number count model, we performed Monte Carlo simulations for the 450 μm images in a way identical to that described in Section 3.2. Because the clustering of faint 450 μm sources on the scales of our beam size is unknown (although likely to be weak), the spatial distribution of our simulated sources is random (cf. Vernstrom et al. 2014 and see discussion therein). For each faint-end count model, 200 simulated images were created using the true noise map, and another 200 using the negative true noise map. The 400 images underwent the same source extraction procedure as the observed image, and 4σ sources were extracted and removed. Since our goal is to constrain the faint-end counts, we only use the central $R < 5'$ deep region, where the noise is less than approximately twice the noise at the map center. We also only used the flux density range within ± 4.2 mJy for the likelihood calculation, so the results are not skewed by the small number of brighter pixels. The resultant PDF averaged from the 400 model images was used as $p(\theta)$ in Equation (5) for the calculation of the log-likelihood.

We calculated the log-likelihood over the parameter space of $\alpha_f = -0.6$ to -6.8 and $S_{\min}$ from 0.0 to 2.75 mJy, with intervals of 0.2 in both. We ignored areas in this parameter space if we observed a trend of monotonically decreasing log-likelihood there toward the extreme parameter values, or if the model overproduces the *COBE* 450 μm EBL measured by Gispert et al. (2000) by factors of more than four. The resultant
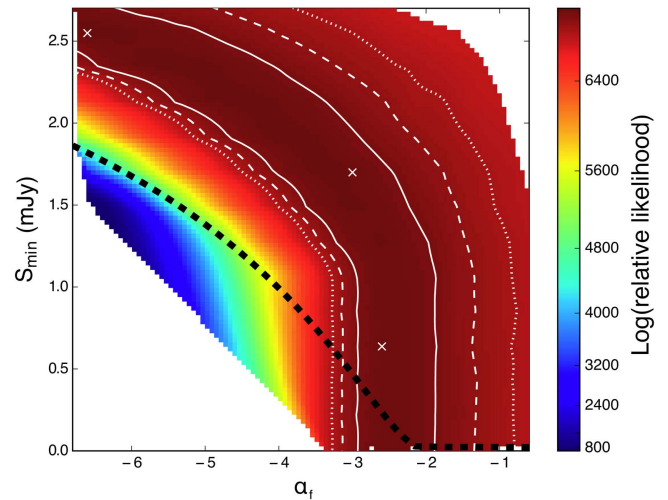

Figure 6. Relative log-likelihood as a function of faint-end slope (α_f) and faint-end termination point ($S_{\min}$) in our fluctuation analysis. The white contours are the 1σ (solid), 2σ (dashed), and 3σ (dotted) confidence ranges. The black dashed curve indicates where the integrated surface brightness becomes 30% higher than the *COBE* EBL measured by Gispert et al. (2000), wherein 30% is the typical uncertainty in the *COBE* measurements (see Section 5.2 for more details). The crosses ([α_f, $S_{\min}$] = [-6.6, 2.55], [-3.0, 1.70], and [-2.6, 0.64]) are picked from the high-likelihood region and their PDFs are shown in Figure 5.

relative log-likelihood distribution is presented in Figure 6. There is a curved "ridge" of high likelihood extending from the upper left to lower right, representing the parameters that can reproduce the observed residual map.

To estimate the confidence levels, we used a bootstrap method. Instead of using the PDF combined from the 400 simulated images for each model, we calculated the PDF and log-likelihood of each simulated image and then determined the dispersion in the log-likelihood. Because we perturbed the number of sources in each flux density bin according to the Poisson distribution in the simulations and adopted both the positive and negative true noise maps, this dispersion represents the variance in the ensemble of images with the same set of model parameters and the underlying noise distribution. It therefore offers an estimate of the confidence range for the likelihood. This is the same method adopted by Scott et al. (2010). Around the maximum likelihood "ridge" in Figure 6, the mean dispersion is 61. We therefore consider the 1σ, 2σ, and 3σ confidence ranges to be 61, 122, and 183 below the maximum log-likelihood, respectively. These are the white contours in Figure 6.

To obtain a rough idea of how the above likelihood method can reproduce the observed residual map, we pick three sets of parameters (white crosses in Figure 6) that are well within the 1σ confidence range and compare their PDFs with the observed one in Figure 5. We find that all three models closely reproduce the PDF of the observed residual map. All of them are clearly different from pure noise. We thus conclude that sources fainter than our 4σ detection limit are needed to explain the background fluctuation in the observed image.

Unfortunately, both Figures 6 and 5 show that a broad range of model parameters can meet the requirement of reproducing the observed low-level fluctuations. The 1σ confidence region in Figure 6 is not localized. Instead, it shows a strong degeneracy between α_f and $S_{\min}$. We can reproduce the observations with a relatively shallower faint-end power-law
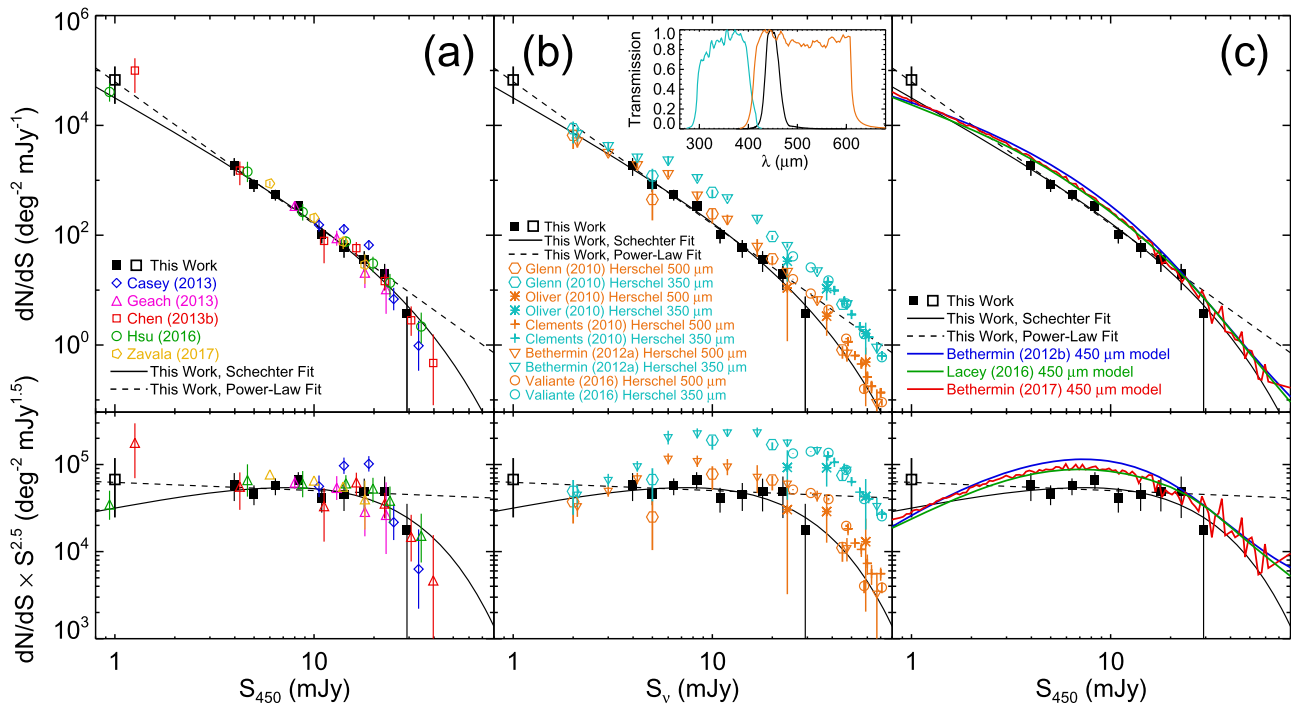
Figure 7. Comparison of 450 μm counts (top panels) and counts renormalized with $S^{2.5}$ to better show the differences and changes in shape (bottom panels). Panel (a) compares the results from this paper and other SCUBA-2 450 μm counts in the literature (Casey et al. 2013; Chen et al. 2013b; Geach et al. 2013; Hsu et al. 2016; Zavala et al. 2017). The solid squares are our counts derived from 4σ sources, while the open square is our count derived from a fluctuation analysis assuming that the faint-end counts extend to $\simeq 1$ mJy (Section 4). The counts derived from various SCUBA-2 surveys are in excellent agreement across the entire flux density range, but the data points are not completely independent (see text). Panel (b) compares our counts with the *Herschel* SPIRE 350 μm and 500 μm counts. The *Herschel* counts were derived from direct source detection at the $\gtrsim 20$ mJy bright end (Clements et al. 2010; Glenn et al. 2010; Oliver et al. 2010; Béthermin et al. 2012a; Valiante et al. 2016), and from stacking analyses (Béthermin et al. 2012a) and $P(D)$ analyses (Glenn et al. 2010) at the faint end. The x-axis shows the flux density measured at the corresponding wavebands, and we do not convert the flux densities to a common wavelength. The inset shows the filter profiles of the SPIRE 350 μm (cyan) and 500 μm (orange) wavebands, and the SCUBA-2 450 μm wavebands (black). Although it is reasonable to expect the 450 μm counts to lie between the 500 μm and 350 μm counts, it is not the case here. At >5 mJy, nearly all *Herschel* counts are consistently above the 450 μm counts. Béthermin et al. (2017) explained this with source clustering at the scales of *Herschel* beam sizes. Panel (c) compares our counts with the 450 μm count models in Béthermin et al. (2012b, 2017) and Lacey et al. (2016).

slope $\alpha_f > -3$ if the counts extend to $S_{min} < 1$ mJy. We can also reproduce the observations with extremely steep power-law slopes ($\alpha_f = -4$ to -6) if the counts terminate at $S_{min} \simeq$ 1.5–2.5 mJy. One can argue that the latter is highly unlikely for two reasons: (1) $\alpha_f < -4$ is much steeper than the power-law slope we observed at the bright-end ($\alpha = -2.59 \pm 0.10$) and (2) observations in the lensing-cluster fields clearly show that the nearly power-law counts should extend to at least 1 mJy (Chen et al. 2013a, 2013b; Hsu et al. 2016; also see Figure 7 and Section 5.1). Below we assume that the counts extend to $S_{min} < 1$ mJy, and we discuss the implication of Figure 6.

At $S_{min} < 1$ mJy, the contours in Figure 6 become vertical. This means that adding sources fainter than 1 mJy to the simulated maps does not improve the results for a fixed power-law slope of $\alpha_f = -2.6^{+0.4}_{-0.7}$. In other words, our data are not sensitive to either a termination or a turnover of the counts if it occurs at <1 mJy. At 1 mJy, the 1σ range of the inferred counts is 2.5×10^4 to 1.2×10^5 deg^{-2} mJy^{-1} (Figure 7). This is consistent with the lensing counts in Chen et al. (2013b) and Hsu et al. (2016), and also consistent with the power-law extrapolation of our bright-end counts. These counts also translate to 0.3–1.4 sources per SCUBA-2 450 μm beam, i.e., sources are highly confused. This is consistent with the confusion limit of approximately 1 mJy estimated by Geach et al. (2013) and explains why our fluctuation analysis is no longer sensitive to sources of <1 mJy. Scott et al. (2010) also

found in their 1.1 mm analyses that adding sources fainter than the limit of roughly one source per beam does not alter the distribution.

To sum up, we do not find evidence of a turnover of the counts between 1 and 3.5 mJy. A single power law with a slope of $\simeq -2.6$ can explain the observations between 1 and 25 mJy. Our fluctuation analysis is insensitive to the counts below 1 mJy as long as the counts maintain a power-law slope between -1.9 and -3.1. A turnover or a sudden termination of the counts below 1 mJy can still be consistent with our data. Indeed, the counts must turn over at some point below 1 mJy, or the integrated surface brightness from the 450 μm sources will exceed the EBL. We will discuss this in Section 5.2.

5. Discussion

5.1. Comparison with Previous Counts

We compare our counts with the previous SCUBA-2 450 μm counts in the literature in Figure 7(a). Among the blank-field surveys, the Geach et al. (2013) and Zavala et al. (2017) surveys reached rms sensitivities of $\lesssim 2$ mJy and 1.2 mJy, respectively, and their survey areas are comparable to ours (i.e., $\simeq 150$ arcmin^2). The Casey et al. (2013) survey covers a large area of ~ 400 arcmin^2 but with a shallower depth of 4.1 mJy. The Geach et al., Casey et al., and our surveys are in the COSMOS field. The Casey et al. survey area fully encloses

ours, as well as that of Geach et al., while our survey area partially overlaps with that of Geach et al. The Zavala et al. survey field is in the Extended Groth Strip, a different line of sight. Both the surveys of Chen et al. (2013b) and Hsu et al. (2016) include lensing-cluster fields of various depths and the COSMOS field for their 450 μm analyses. For COSMOS, both teams used the data taken by Casey et al. The three cluster fields in Chen et al. with 450 μm data are all included in Hsu et al., who added additional integrations and also two further clusters. The sensitivities of the lensing-cluster surveys are determined by the amplification factors of the lensed sources rather than the instrumental noise. Because of the overlapping of data and survey fields, the results in these papers are not completely independent of each other, except for those in Zavala et al.

At the very bright end of $\gtrsim 30$ mJy, all of the SCUBA-2 counts are consistent with each other and show a steeper fall-off. Here, our count has a large error because of our smaller effective area. At the roughly 1 mJy faint end, our results derived from the fluctuation analysis and the extrapolation from our bright-end counts are both consistent with the lensing results of Chen et al. (2013b) and Hsu et al. (2016). As we mentioned in Section 4, there is no evidence for a faint-end turnover in our data above 1 mJy. The two lensing data points at about 1 mJy seem consistent with this.

The counts are best constrained in our data below between $\gtrsim 3$ mJy (the intrinsic flux density of our faintest detected source) and 25 mJy. Here, our results are consistent with previous ones within the error bars of each individual data point, except for those between 10 and 20 mJy from the shallower survey of Casey et al. (2013), which are higher than the other counts. Cosmic variance (i.e., the effects of clustering on small fields) does not easily explain the elevated counts in Casey et al. since their survey field fully encloses ours and that of Geach et al. For cosmic variance to be the explanation, the >10 mJy sources would have to be strongly clustered at $5'$ scales. Unfortunately, there does not exist a deep and wide-field 450 μm data set to test such clustering. A hint of clustering can be found in Casey et al. (2015; also see Wang et al. 2016), who detected a filamentary structure at $z = 2.47$ in their SCUBA-2 image. This structure, represented by their seven SCUBA-2 sources, runs through our field. Five of their sources are within our survey area and all of them are detected by us. Therefore, this structure cannot be responsible for the difference between our counts and the counts in Casey et al. (2013). Hung et al. (2016) reported another $z \sim 2.1$ large-scale structure in this field. However, the only galaxy with a 450 μm detection in their sample is detected by both Casey et al. (2013) and us. So, this structure does not seem to drive the higher counts in Casey et al. (2013), either.

In order to more quantitatively compare the counts in these surveys, we refitted the counts quoted by the various authors and derived the counts at 6 and 10 mJy and the associated uncertainties. The results are presented in Table 3. The dispersions in these values are 127 and 18 deg^{-2} mJy^{-1} at 6 mJy and 10 mJy, respectively, or 21% and 10% relative to the mean. These are comparable to the shot noise in the counts, showing that the field-to-field variance should be even smaller. We further tested this using the simulated 2 deg^2 450 μm catalog of Béthermin et al. (2017), which contains source clustering, to conduct simulations of source extraction and number counts (see Appendix B for details). We found a scatter of about 10% in the

Table 3
Comparison of 450 μm Counts

Authors	dN/dS (6 mJy) (deg^{-2} mJy^{-1})	dN/dS (10 mJy) (deg^{-2} mJy^{-1})
This work[a]	602.2 ± 66.8	160.4 ± 18.6
Geach et al. (2013)[b]	747.0 ± 165.0	180.3 ± 18.4
Casey et al. (2013)[b]	...	180.5 ± 28.4
Chen et al. (2013b)[a]	530.7 ± 172.0	145.7 ± 30.5
Hsu et al. (2016)[a]	563.7 ± 85.5	170.6 ± 24.7
Zavala et al. (2017)[b]	827.9 ± 64.4	196.9 ± 19.5

Notes.
[a] Power-law fits are adopted.
[b] Schechter fits are adopted.

counts between 6 and 10 mJy for our field size. Therefore, both the existing data and the simulations of Béthermin et al. (2017) do not indicate a field-to-field variance that is much larger than 20% for 450 μm sources. However, we caution that the scatter seen in Table 3 is not exactly the field-to-field variance, since the some of the fields overlap, and the Chen et al. and Hsu et al. results are combined from multiple fields. This might underestimate the field-to-field variance, since counts from different fields are combined and averaged in these studies. A more proper evaluation of the field-to-field variance will be provided by the S2CLS 450 μm surveys (J. E. Geach et al. 2017, in preparation), along with the few 450 μm lensing fields. Nevertheless, it is still quite remarkable that the various 450 μm counts agree with each other at the roughly 20% level.

Geach et al. (2017) reported a roughly 50% field-to-field scatter for 850 μm sources in S2CLS, the field sizes of which are 0°.5 to 1°. The scatter is still roughly 50% when the S2CLS 850 μm counts are measured over $10'$ fields at 3.5 mJy, of which roughly 60% is contributed by the Poisson errors in such smaller fields (J. Geach 2017, private communication). Both of these results are much larger than the scatter we see in the 450 μm counts. This suggests that the 450 μm sources are less clustered at scales larger than our field size ($\gtrsim 8$ Mpc at $z = 2$). Two factors may contribute to this. First, 850 μm surveys are only sensitive to the most luminous dusty galaxies because of the confusion limit, while 450 μm surveys can reach sources with lower luminosities (i.e., weaker clustering). However, the source densities listed in Table 3 are not yet at the limit of the 850 μm SCUBA-2 surveys. Therefore, this is unlikely to be a luminosity effect. Another reason is the strong negative K-correction at 850 μm, making the 850 μm band very sensitive to luminous dusty galaxies at $z > 2$. Wilkinson et al. (2017) show that such high-redshift SMGs are clustered more strongly than those at lower redshifts. Such high-redshift SMGs are less abundant in 450 μm images. This is evident in the redshift distributions of the 450 and 850 μm sources (Casey et al. 2013). It is therefore possible that the larger field-to-field variance at 850 μm is driven by the high-redshift SMGs.

In Figure 7 (b), we show a comparison between our 450 μm counts and the *Herschel* SPIRE 350/500 μm counts, along with the filter profiles of these three passbands. Given the passbands, it is reasonable to expect the 450 μm counts to fall between the 350 and 500 μm ones, and probably closer to the 500 μm ones. To our surprise, this is not the case, and the 450 μm counts fall below both the *Herschel* 350 and 500 μm counts. The *Herschel* confusion limit is approximately 20 mJy in both wavebands. The counts at >20 mJy were derived with

direct source extraction (Clements et al. 2010; Glenn et al. 2010; Oliver et al. 2010; Béthermin et al. 2012a; Valiante et al. 2016), while the counts at <20 mJy were derived by stacking *Spitzer* 24 μm sources in the *Herschel* images (Béthermin et al. 2012a) and from $P(D)$ analyses (Glenn et al. 2010). The *Herschel* counts derived by various authors are highly consistent with each other, regardless of how they were derived. All of them lie significantly above the SCUBA-2 450 μm counts over nearly the entire flux density range of interest. The 500 μm data points are individually about 1σ to 2σ away from the SCUBA-2 counts; however, the fact that collectively nearly all of them are above the SCUBA-2 points means that the overabundance in the *Herschel* counts is significant. In the literature, overabundant *Herschel* counts were already noted by Chen et al. (2013b), but Geach et al. (2013) and Zavala et al. (2017) considered the *Herschel* counts to be consistent with their SCUBA-2 counts, perhaps because of the larger error bars and sparse data points. With our better constrained SCUBA-2 450 μm counts, it should now be clear that there is a discrepancy with the *Herschel*-derived counts.

Béthermin et al. (2017) offered an explanation for the elevated *Herschel* counts. With simulations of dark matter halos in a 2 deg^2 light cone, an abundance-matching technique to populate the halos with galaxies, and models of star formation and galaxy SEDs, these authors can reproduce the observed *Herschel* counts with much lower intrinsic counts. They therefore attribute the elevated *Herschel* counts to source blending in the *Herschel* images, caused by the clustering of FIR sources and the large *Herschel* beam in the SPIRE bands. We note that blending alone does not necessarily bias the $P(D)$ analyses and stacking analyses in the faint end, as the associated simulations would have accounted for its effects. However, the simulations typically do not include source clustering, which can amplify the observed image fluctuation and the stacking signal.

Béthermin et al. (2017) also show that the intrinsic counts are much closer to the SCUBA-2 counts, because the SCUBA-2 450 μm beam is much smaller. Despite this, in Figure 7(c), we show that the 450 μm counts predicted by Béthermin et al. (2017), as well as by Lacey et al. (2016), are somewhat higher than the SCUBA-2 counts at flux densities above 3 mJy. The overprediction in the counts is up to about 70% in the Béthermin et al. (2017) case. The slopes of the counts at flux densities below 3 mJy is also shallower in the models than what the observations suggest. The above 70% offset in counts can be translated to a 23% offset in flux, which is much larger than the generally expected 12% calibration uncertainty in SCUBA-2 observations (Dempsey et al. 2013). In addition, the offset between the model counts and observed counts is not a constant. It is not possible to explain this offset with a simple calibration error. The discrepancy between the models and observations thus appears to be real. Nevertheless, the work of Béthermin et al. (2017) and the comparisons in our Figure 7(b) highlight the importance of high angular resolution in studying high-redshift galaxies. The beam size of SCUBA-2 at 450 μm is much less affected by clustering (Appendix B) and can therefore provide much more robust measurements of both the spatial density and flux density of sources.

Finally, we estimate the bias in the *Herschel* 500 μm counts, assuming that our 450 μm counts are unbiased. At around 10 mJy, the observed *Herschel* 500 μm counts are higher than our 450 μm counts by 1.25 times in flux density, or by 1.8

times in number density. These are lower limits for the bias in the *Herschel* counts, since 500 μm counts should be intrinsically lower than 450 μm counts. Estimating the intrinsic offset between the 450 and 500 μm counts requires knowledge about the S_{450}/S_{500} flux density ratios of the sources, which are determined by their redshift distribution and SEDs. A zeroth-order estimate can be made through the model of Béthermin et al. (2017). Although Figure 7(c) shows that the model does not perfectly match the 450 μm counts, it nevertheless predicts 450 μm counts that lie between the 350 and 500 μm counts, meaning that the S_{450}/S_{500} flux density ratios in its source catalog are not too far off. If we use the intrinsic offset between the 450 and 500 μm counts in the model of Béthermin et al. (2017) to adjust the above observed offset, we then find that the observed *Herschel* 500 μm counts should be higher than the intrinsic 500 μm counts by roughly 1.4 times in flux, or 2.5 times in number density, at flux densities of about 10 mJy.

5.2. Contributions to the 450 μm EBL

We compare the 450 μm EBL resolved in our SCUBA-2 observations with various *COBE* EBL measurements. The low angular-resolution satellite EBL measurements and resolved source counts contain different sets of systematics. Comparing them, as well as testing them against each other, provides insight into the nature of the sources that give rise to the EBL.

The 450 μm EBL estimations based on the *COBE* FIRAS experiment are 109 Jy deg^{-2} (Puget et al. 1996), 142 Jy deg^{-2} (Fixsen et al. 1998), and 150 Jy deg^{-2} (Gispert et al. 2000). The uncertainty in them is about 30%. The difference among these results arises from the subtractions of the foregrounds and should be considered as a measure of systematic uncertainty. In the subsequent discussion, we compare our resolved EBL with the full range of 109–150 Jy deg^{-2} from the above *COBE* results.

We show the 450 μm surface brightness integrated from our source counts in Figure 8. For this calculation, we adopted our Schechter fit above 10 mJy and our power-law fit for 0.1–10 mJy. For uncertainty estimation, we perturbed our counts according to their errors, re-conducted the fitting, and calculated the dispersion in the results. Down to 3.5 mJy, which is the corrected flux density of our faintest 4σ source, we resolved 35.5 ± 4.3 Jy deg^{-2} of the 450 μm EBL (black solid curve in Figure 8). This corresponds to 24% ± 3% to 33% ± 4% of the total EBL, depending on which EBL estimate we adopt. If we integrate down to 1 mJy, where we have constraints on the counts from our fluctuation analysis, we obtain a value of 90.0 ± 17.2 Jy deg^{-2} (black dashed curve in Figure 8), corresponding to 60% ± 11% to 83$^{+15}_{-16}$% of the EBL.

If we continue the integration with the same power-law slope, we will reach 100% resolution of the EBL from Puget et al. (1996) at 0.77 mJy, while in order to fully account for the EBL from Gispert et al. (2000), the counts have to extend to approximately 0.48 mJy with the same faint-end slope. Roughly speaking, the flux of 0.48 mJy corresponds to infrared luminosities of 3.8 × 10^{10} $L_{\odot}$ and 7.9 × 10^{10} $L_{\odot}$ at $z = 1$ and $z = 2$, respectively, if we assume the luminosity-dependent dust SEDs of J. K. Chu et al. (2017, in preparation), which incorporate the latest *WISE* and *Herschel* photometry for local infrared-selected galaxies (Chu et al. 2017). The luminosity would be 30% ($z = 2$) to 40% ($z = 1$) higher if we assume the median SED of bright 870 μm-selected SMGs in Danielson
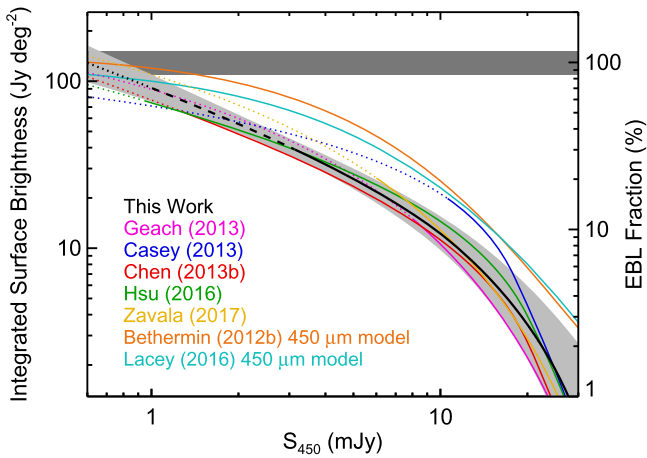
Figure 8. Integrated 450 μm surface brightness from various SCUBA-2 surveys. The dark shaded area shows the range of 450 μm EBL values inferred from various *COBE* studies. The black curve is the result derived from our 450 μm counts, and the light shaded area is its uncertainty range. The colored curves are results from previous 450 μm surveys. The solid portions of the curves represent counts constrained by detected sources, while the dotted portions represent the faint-end extrapolations of the counts. The dashed portion of the black curve is where our counts are constrained through the fluctuation analysis. The models of Béthermin et al. (2012b) and Lacey et al. (2016) are also shown for comparison. The right-hand *y*-axis is the fraction of the resolved EBL, and the 100% resolution level is set to be the midpoint between the minimum and maximum values among the *COBE* determinations.

et al. (2017), because such luminous SMGs have higher dust temperature and therefore more emission from $\lesssim 200$ μm. The luminosity of 3.8–7.9×10^{10} $L_\odot$ corresponds to an SFR of roughly 6–13 $M_\odot$ yr^{-1}. These are in the regime of the typical SFR of rest-frame UV-selected high-redshift galaxies.

The above assumes that the extension of the counts below 1 mJy maintains a power-law slope of $\alpha_f = -2.6$. A more likely scenario is that the counts become shallower below 1 mJy. Shallower (Schechter) slopes in the UV luminosity functions are typical for faint rest-frame UV-selected populations, ranging from -0.8 to -1.7 at $z \simeq 1.7$ to 3 (Steidel et al. 1999; Sawicki & Thompson 2006; Reddy & Steidel 2009). Steeper slopes are observed at higher redshifts: -1.6 at $z \simeq 4$ (Bouwens et al. 2015) and -2.0 at $z \simeq 6$–8 (Bouwens et al. 2015, 2017), but are still shallower than the slope we observed on 450 μm sources.

Another hint of a shallower slope in the extreme faint end comes from ALMA imaging at longer wavelengths. Recent ALMA observations reported nearly full resolution of the 1.1 mm EBL with serendipitous detections of faint sources (Fujimoto et al. 2016) and stacking analyses (Aravena et al. 2016; Wang et al. 2016; Dunlop et al. 2017). Roughly speaking, it requires the detections of $S_{1100} \simeq 0.01$–0.02 mJy sources to achieve a full resolution of the 1.1 mm EBL. For $z \simeq 1$–2, these sources would have 450 μm fluxes of about 0.1–0.2 mJy, a few times fainter than the above 0.48 mJy extrapolated based on a constant slope. This again suggests a slope shallower than -2.6.

Our STUDIES survey was allocated 330 hr of observations (including some overheads). Roughly 40% of the observations were carried out in the first year and included in this paper. Once the survey is complete, we can expect to detect sources with intrinsic flux densities of $\gtrsim 2$ mJy in the deepest region and directly resolve around 55 Jy deg^{-2} of the EBL (30% to 50%). Furthermore, an extension of STUDIES was recently approved

to conduct equally deep pointing in the Subaru/*XMM-Newton* Deep Survey field (Furusawa et al. 2008). Both the increases in depth and survey area will lead to dramatically improved source counts in the 2–30 mJy bright end. The deeper image may enable meaningful fluctuation analysis below 2 mJy with more model parameters than our current simple two-parameter model. If this is the case, better constraints in the 1–2 mJy regime may help narrow down the parameter space for the extremely faint end below 1 mJy (e.g., a shallower slope and/ or a turnover flux density). It will be interesting if the improved fluctuation analysis can reach the >100% resolution of the *COBE* EBL, and hence start to pin down the EBL better than the satellite estimates. The most robust EBL estimate will likely require extremely deep and wide interferometric imaging in the future.

6. Summary

In our JCMT Large Program STUDIES, we are carrying out extremely deep 450 μm imaging with SCUBA-2 in the COSMOS-CANDELS region. The 7″ resolution of the 450 μm band provides the opportunity to probe beyond the conventional 850 μm confusion limit to detect fainter galaxies. Our goal is to detect faint 450 μm sources close to the confusion limit of SCUBA-2 to study a representative sample of the high-redshift FIR galaxy populations that give rise to the bulk of the FIR background and the cosmic star formation. With the first year of STUDIES data, we reached a noise of 0.91 mJy at the map center for point sources, about 30% deeper than the previous deepest 450 μm map, and covered a deep area of $R = 7\rlap{.}'5$. We detected 98 and 141 sources at 4.0σ and 3.5σ, respectively. Our source counts are best constrained between 3.5 and 25 mJy (4σ), and are consistent with most of the previous counts derived from blank-field and lensing-cluster surveys. The field-to-field variance among the various surveys is about 20%, much smaller than the variance observed in 850 μm surveys, perhaps suggesting weaker clustering in the 450 μm population at scales larger than our field size. In this flux density range, our counts are consistent with a power law with a slope of $\alpha = -2.59 \pm 0.10$. We further constrain the counts at 1–3.5 mJy with a fluctuation analysis. We see evidence of a termination or turnover of the faint-end counts between 1 and 3.5 mJy. The power-law slope at 1–3.5 mJy is $\alpha_f = -2.6^{+0.4}_{-0.7}$, consistent with the slope at >3.5 mJy. This is also consistent with the counts at around 1 mJy derived from previous lensing-cluster surveys. On the other hand, our counts and all other SCUBA-2 450 μm counts appear significantly lower than *Herschel* counts at 350 and 500 μm. This discrepancy is likely caused by source blending under the coarse *Herschel* beam, amplified by source clustering at the scales of the beam. Because of its higher angular resolution, SCUBA-2 counts at 450 μm do not suffer from these effects. Our extremely deep SCUBA-2 map has resolved a substantial fraction of the 450 μm EBL estimated by *COBE*, 24% ± 3% to 33% ± 4% from the 4σ sources at >3.5 mJy, and 60% ± 11% to 83^{+15}_{-16}% if we include the 1–3.5 mJy faint-end counts derived from the fluctuation analysis. STUDIES is an ongoing survey, and we expect that our future deeper image can be used to better determine the EBL at 450 μm as well as providing accurate counts for constraining galaxy evolution models.

We thank the JCMT/EAO staff for the observational support and the data/survey management, Oliver Doré and Matthieu

Appendix A
Flux Boosting, Completeness, Spurious Fraction, and Source Blending

The procedure for deriving true counts (Section 3.2) treats the observational effects of flux boosting, completeness, spurious sources, and blending simultaneously. This is different from some other works in the literature (e.g., Casey et al. 2013; Chen et al. 2013a; Geach et al. 2013; Zavala et al. 2017). Previous 450 μm studies did not deal with the effects of source

blending, partially because they were relatively shallow and the probability of chance projections was lower. The smaller 450 μm beam also makes it less likely for two sources to blend with each other (e.g., Cowley et al. 2015), unlike the case for longer wavebands (Wang et al. 2011; Hodge et al. 2013; Karim et al. 2013; Simpson et al. 2015b). Later, we will show that source blending is not entirely negligible in our deep image. For the other effects, previous studies estimated the amplitude of the corrections through simulations similar to ours and applied these corrections to the observed flux densities and counts. The correction to the counts typically looks like

$$C_{\rm corr}(S_{\rm corr}) = C_{\rm raw}(S_{\rm obs}) \times \frac{(1 - \mathcal{F}_{\rm spu}(S_{\rm obs}))}{\mathcal{F}_{\rm comp}(S_{\rm corr})}, \qquad (6)$$

where $\mathcal{F}_{\rm spu}$ is the fraction of spurious sources and $\mathcal{F}_{\rm comp}$ is the detection completeness fraction. To derive the two $\mathcal{F}$ terms and the conversion between $S_{\rm obs}$ and $S_{\rm corr}$, one normally has to assume a one-to-one relation between an output source and an input source in the simulation. The possibility of source blending makes this assumption no longer valid. We avoid this and do not attempt to correct the observed counts using Equation (6). Instead, we fully rely on the iterative procedure and Equation (1), described in Section 3.2, to derive the intrinsic counts. However, we can still estimate these effects using our simulations in order to obtain a picture of our observation and source extraction efficiency, and to compare with previous studies.

To estimate flux boosting caused by the Eddington bias and faint confusing sources, we matched sources in the input and output catalogs of our simulations. For each output source, we searched for input sources within a radius of a beam HWHM. We consider that we have a match when the flux densities of the input and output sources are within a factor of two of each other. This ensures that the input and output sources have similar flux densities, since for any output source, it would be possible to associate it with an arbitrarily faint nearby input source, given that faint sources have much higher spatial density (we will come back and discuss the choice of this factor of two at the end of this section). When there are multiple input sources meeting the above distance and flux ratio criteria, the brightest one is considered as the match. We started from the brightest output source and moved down the list. The matched input sources were not considered in the subsequent searches. We repeated this for the 200 realizations. The output-to-input flux ratio of each matched pair is the flux boosting factor. Figure 9 shows the flux boosting factor as a function of the output (observed) source flux density (panel a) and the input (intrinsic) source flux density (panel b). Overall, the required correction for measured flux densities is around 20% in panel (a). Panel (b) shows that sources as faint as about 2 mJy (intrinsic) can be strongly boosted into our 4σ detection range at $\gtrsim$4 mJy, but with very low detection completeness (panel c). The flux boosting factor in (b) is artificially capped at 2.0 for the faintest sources because we require the flux densities of the input and output sources to be within this factor. However, the curves do not suggest a much higher boosting factor if we remove this requirement.

To estimate the completeness and spurious fraction, we only considered input sources that have a chance of being detected, given the noise levels at their locations. This is necessary because our map has a highly non-uniform sensitivity
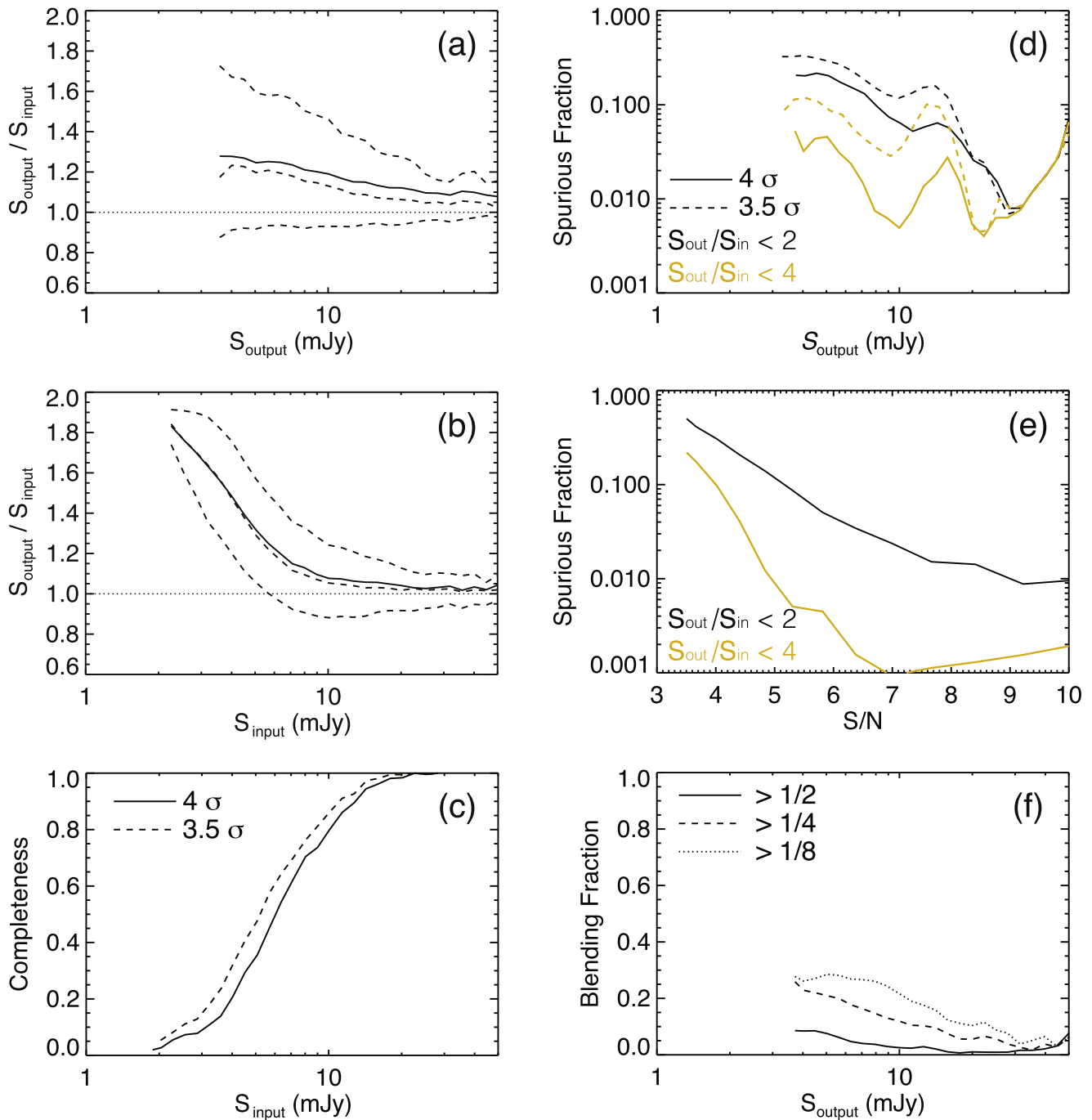
Figure 9. Bias effects in the observations and source extraction. Panel (a) shows the flux boosting factor vs. output (observed) source flux density. Panel (b) shows the flux boosting factor vs. input (intrinsic) source flux density. In both (a) and (b), the solid curves are the mean values, while the dashed curves are the 68th ($\pm 1\sigma$) and 50th percentile (median) values. The overall boosting correction for measured flux densities is around 20%. A small number of intrinsically faint sources ($S_{input} \gtrsim 2$ mJy) can be strongly boosted into our detection range. Panel (c) shows the completeness vs. input (intrinsic) source flux density for a 4σ detection threshold (solid curve) and a 3.5σ detection threshold (dashed curve). Panel (d) shows the spurious fraction vs. output (measured) flux density. The spurious fraction for 4σ detections is shown with the solid curve, and for 3.5σ detections with the dashed curve. Panel (e) shows the spurious fraction vs. detection S/N. In both (d) and (e), the black and yellow curves are derived by requiring the matched input and output sources to have flux density ratios less than 2 and 4, respectively. The difference between the yellow and black curves shows that the required correction for spurious sources sensitively depends on the details of the matching between the input and output source lists. Panel (f) shows the fraction of observed sources that are blends of multiple sources. The three curves represent the cases where the flux densities of the blended sources in the input list are at least 1/2, 1/4, and 1/8 of the flux densities of the detected sources. The 1/4 curve best represents the fraction of multiple sources to be found in sensitive interferometric follow-up, if the sources are not clustered at $\sim 10''$ scales.

distribution. To perform this estimate, we used the $+1\sigma$ flux boosting factor in Figure 9(a) to boost the flux densities in the input source list. Only those sources with boosted flux densities greater than 3.5 times and 4 times the local rms noise are considered, corresponding to 3.5σ and 4σ detection thresholds.

We then matched the sources in the input and output catalogs using the same criteria as for the flux boosting estimate. An output source without a match is considered spurious (although its flux may still be real, contributed by multiple fainter sources). An input source without a match is considered

undetected (although it may contribute flux to a nearby source). The detection completeness calculated this way is presented in Figure 9(c) for sources detected at $>4\sigma$ and $>3.5\sigma$. The spurious rate is presented in Figures 9(d) and (e) (black curves) as functions of the output (measured) flux density and detection S/N, respectively.

In Figure 9(e), we see that the spurious fraction for $\sim 3.5\sigma$ sources is approximately 50%. Even at $\sim 4\sigma$, the fraction is approximately 30%. Both values appear somewhat high. However, sources detected with such a low S/N only comprise a small fraction in our sample. Figure 9(d) better reflects the overall spurious fraction, as here sources detected at different S/N levels are mixed according to the realistic counts and sensitivity distribution of the map. In Figure 9(d), there is a small bump in spurious fractions between 10 and 20 mJy. This is because some of these brighter sources are detected in the outer area where noise increases rapidly. For $>4\sigma$ detections, the spurious rate is below 15% above 7 mJy and below about 20% in nearly the entire flux density range of interest. If we lower the threshold to 3.5σ, the completeness would increase by almost a factor of two at the faint end of 3–4 mJy, but the spurious rate would also increase to 35%. Given this, it is not obvious to us whether we should favor 3.5σ detections over 4σ detections for number count estimates. Furthermore, because of the nature of our Equation (1), the choice of detection threshold will not change the corrected source counts; it will only slightly change the interpretation of the intrinsic flux density range over which the counts are measured.

We compare the above results with other SCUBA-2 450 μm surveys and do not find major discrepancies. Our flux boosting factor of 20% is comparable to those in Casey et al. (2013) and Chen et al. (2013a), but seems much higher than that in Zavala et al. (2017, their Figure 3). The very low flux boosting factor in Zavala et al. might be caused by the difference in how the simulations were conducted. The behavior of the completeness curves in Figure 9(c) is qualitatively similar to those presented by other authors (Casey et al. 2013; Geach et al. 2013; Zavala et al. 2017). The differences in sensitivities and mapping strategies prevent further quantitative comparison. Our spurious rates of 20%–40% near the detection limit is also comparable to that in Casey et al. (2013).

Finally, to obtain a rough idea of source blending, we estimated the fraction of output sources that consist of multiple blended faint sources. We again conducted source matching with a search radius of half a beam FWHM. However, this time, for each output source, we consider input sources that are brighter than 1/2, 1/4, and 1/8 times the output flux density. Figure 9(f) shows the fraction of output sources that contain contributions from more than one input source that meet the above flux ratio thresholds. The ">1/2" curve (solid) represents cases where sources of nearly equal brightness are blended and detected; these are rare, and the blending fraction does not exceed 10%. The ">1/4" curve (dashed) probably better mimics the multiple fractions to be found in sensitive interferometric surveys, since the aimed detection S/N for the single-dish fluxes is typically between 10 and 20, and a four times fainter companion can be detected at $>3\sigma$. This suggests that we will find roughly 10%–20% of our sources to be multiples if we conduct deep ALMA Band 9 imaging follow0up. The majority of the multiple sources are pairs, and blends of more than three sources only account for 6% of these. This predicted multiple fraction is much lower than the

35%–60% multiple fractions typically found in the interferometric follow-up of 850 μm SCUBA-2 and LABOCA sources (Barger et al. 2012; Hodge et al. 2013; Simpson et al. 2015a), This is a consequence of the smaller SCUBA-2 beam at 450 μm. Nevertheless, the fraction of 10% to 20% is comparable to the error in the amplitudes of our counts, meaning that its effect is not negligible below 10 mJy. The ">1/8" curve (dotted) steeply rises from above 20 mJy to below 10 mJy, but artificially saturates at 6 mJy because we do not include <1 mJy sources in our simulations.

We point out that the results presented in this section are highly sensitive to the details of the source matching criteria between the input and output lists. For example, if we allow the flux density ratio between the matched input and output sources to be greater than two (i.e., make it easier to find a match), we can artificially decrease the spurious fraction, increase the flux boosting factor, and extend the derived intrinsic counts to fainter flux density limits. To demonstrate this, we show the spurious fraction derived with the input and output flux ratios relaxed to 4 in Figures 9(d) and (e) with yellow curves. For 4σ detections, the spurious fraction is below 5% over nearly the entire flux density range, but many of the added detections have flux densities that are dramatically boosted (more than a factor of two). We stress again that we do not base our source count correction on the corrections of flux boosting, completeness, and spurious sources, because of all of the above ambiguities and the arbitrariness in the choice of source matching criteria.

Appendix B
Effect of Clustering

The results in the previous section are a strong indication that our counts will be biased if we do not properly take source blending into account when we correct the observed counts using Equation (6). Our Equation (1) does not suffer from this complication. On the other hand, our simulations (as well as similar simulations in the literature) assume a random (unclustered) spatial distribution. Our counts will still be biased if the clustering of the 450 μm sources at the 10″ scale (20 comoving kpc) is strong enough to alter the blending fraction. The simulations of Cowley et al. (2015) and Béthermin et al. (2017) show that clustering is not likely to have a strong effect on the observed counts for our beam size. The ALMA observations of the 870 μm single-dish selected sources of Hodge et al. (2013) seem to also support weak or no clustering at such small scales. Future ALMA observations of 450 μm sources are needed to further test the small-scale clustering in the 450 μm population. In the meantime, we use the simulations of Béthermin et al. (2017), which include clustering effects, to test whether clustering would bias our results.

We used the 2 deg^2 light cone provided by Béthermin et al. (2017) and the associated 450 μm fluxes of the simulated sources. The general procedure is identical to our simulations described in Section 3.2, except that we use sources in Béthermin et al. (2017) for the input. We convolved the simulated sources with our SCUBA-2 PSF and randomly pick a location in the 2 deg^2 region to simulate an observed image. This is repeated 100 times each for the positive and negative true noise maps. We performed source extraction over the 200 simulated maps and derived the raw (observed) source counts. The results represent the observed counts where sources are
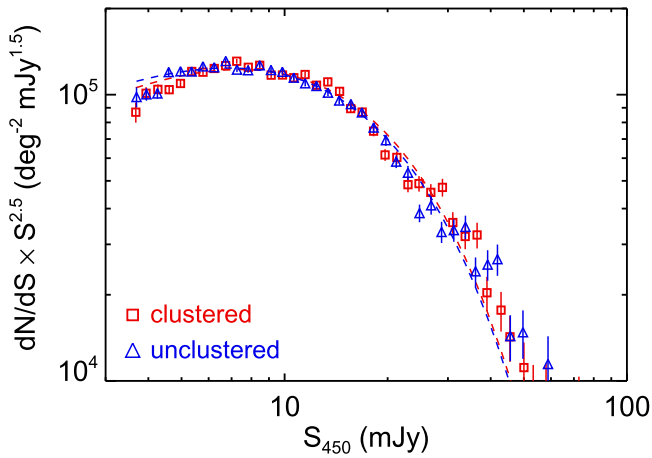
Figure 10. Raw SCUBA-2 450 μm counts derived with the simulations of Béthermin et al. (2017). The red symbols are the results with source clustering and the blue symbols without clustering. The dashed curves are Schechter fits to the counts.
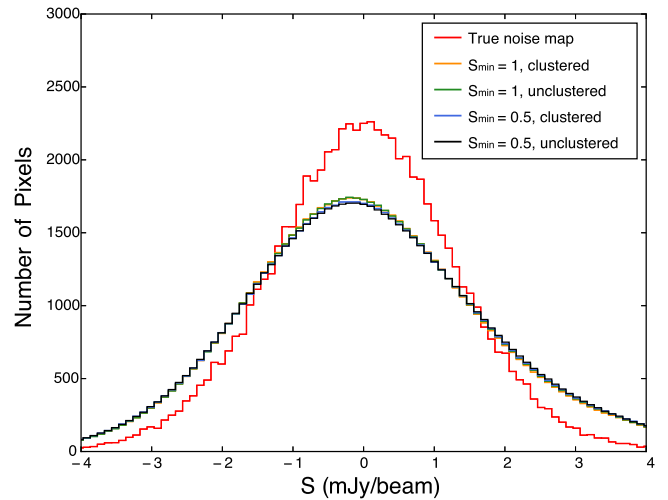

Figure 11. Distributions of pixel brightness in the residual maps from the simulations using the light cone of Béthermin et al. (2017) and the true noise map (red). For both $S_{min} = 0.5$ and 1.0, the distributions for the clustered and unclustered cases are nearly identical. The differences in the log-likelihood are also negligible.

clustered and are shown with the red symbols and curve in Figure 10. We then randomized the positions of the simulated sources in the 2 deg^2 region and repeated the procedure. The results represent the observed counts where sources are not clustered but they have identical intrinsic counts, and they are shown with blue symbols and curve in Figure 10. With the fitted Schechter functions (dashed curves), we find that at 5, 10, and 20 mJy, the counts with clustering are higher than the unclustered cases by -3.2%, $+0.6\%$, and $+3.6\%$, respectively. These are essentially negligible and do not suggest a systematic bias caused by source clustering. By observing the data points in Figure 10, it is apparent that the accuracy of this test is limited by the size of the light cone as well as the area coverage of our observations. We thus confirm that our counts are not biased by clustering, thanks to the small beam size of SCUBA-2 at 450 μm.

Next, we test whether clustering would bias the fluctuation analyses for the faint end. We again use the simulations of Béthermin et al. (2017), with the original simulated source positions for the clustered case and randomized source positions for the unclustered case. The procedure is identical to that described in Section 4. For simplicity, we tested the cases with faint-end cutoffs of $S_{min} = 0.5$ and 1.0 mJy. We created 400 simulated maps for each case and calculate the log-likelihood against the observed residual map. The pixel brightness distributions of the simulated residual maps are shown in Figure 11. For $S_{min} = 1.0$ mJy, the dispersions of the log-likelihoods of the 400 simulated maps are 104 (clustered) and 73 (unclustered), while the mean difference between the clustered and unclustered log-likelihoods is 37. For $S_{min} = 0.5$ mJy, the dispersions of the log-likelihoods are 109 (clustered) and 89 (unclustered), while the mean difference between the clustered and unclustered log-likelihoods is 25. In both cases, the difference induced by source clustering is much smaller than the variance in the ensemble of simulated images. This can also be seen in Figure 11, where the clustered and unclustered curves essentially overlap, and the difference caused by clustering is much smaller than changing the cutoff flux. Based on these, we conclude that our fluctuation analyses are not likely to be biased by source clustering at the scale of the SCUBA-2 450 μm beam.

ORCID iDs

Wei-Hao Wang ⓘ https://orcid.org/0000-0003-2588-1265
Ian Smail ⓘ https://orcid.org/0000-0003-3037-257X
Tadayuki Kodama ⓘ https://orcid.org/0000-0002-2993-1576
Omar Almaini ⓘ https://orcid.org/0000-0001-9328-3991
Yiping Ao ⓘ https://orcid.org/0000-0003-3139-2724
Andrew W. Blain ⓘ https://orcid.org/0000-0001-7489-5167
Chian-Chou Chen ⓘ https://orcid.org/0000-0002-3805-0789
David L. Clements ⓘ https://orcid.org/0000-0002-9548-5033
Christopher J. Conselice ⓘ https://orcid.org/0000-0003-1949-7638
Linhua Jiang ⓘ https://orcid.org/0000-0003-4176-6486
Rob J. Ivison ⓘ https://orcid.org/0000-0001-5118-1313
Woong-Seob Jeong ⓘ https://orcid.org/0000-0002-2770-808X
Kotaro Kohno ⓘ https://orcid.org/0000-0002-4052-2394
Xu Kong ⓘ https://orcid.org/0000-0002-7660-2273
Minju Lee ⓘ https://orcid.org/0000-0002-2419-3068
Iván Oteo ⓘ https://orcid.org/0000-0001-5875-3388
Douglas Scott ⓘ https://orcid.org/0000-0002-6878-9840
Xin Wen Shu ⓘ https://orcid.org/0000-0002-7020-4290
James M. Simpson ⓘ https://orcid.org/0000-0002-8521-1995
Yoshiki Toba ⓘ https://orcid.org/0000-0002-3531-7863
Jun-Xian Wang ⓘ https://orcid.org/0000-0002-4419-6434
Julie L. Wardlow ⓘ https://orcid.org/0000-0003-2376-8971

References

Alexander, D. M., Bauer, F. E., Chapman, S. C., et al. 2005, ApJ, 632, 736
Almaini, O., Scott, S. E., Dunlop, J. S., et al. 2003, MNRAS, 338, 303
Aravena, M., Decarli, R., Walter, F., et al. 2016, ApJ, 833, 68
Asboth, V., Conley, A., Sayers, J., et al. 2016, MNRAS, 462, 1989
Barger, A. J., Cowie, L. L., Chen, C.-C., et al. 2014, ApJ, 784, 9
Barger, A. J., Cowie, L. L., & Richards, E. A. 2000, AJ, 119, 2092
Barger, A. J., Cowie, L. L., Sanders, D. B., et al. 1998, Natur, 394, 248
Barger, A. J., Cowie, L. L., & Sanders, D. B. 1999, ApJL, 518, L1
Barger, A. J., Wang, W.-H., Cowie, L. L., et al. 2012, ApJ, 761, 89
Baugh, C. M., Lacey, C. G., Frenk, C. S., et al. 2005, MNRAS, 356, 1191
Béthermin, M., Daddi, E., Magdis, G., et al. 2012b, ApJL, 757, L23
Béthermin, M., Le Floc'h, E., Ilbert, O., et al. 2012a, A&A, 542, A58
Béthermin, M., Wu, H.-Y., Lagache, G., et al. 2017, A&A, submitted (arXiv:1703.08795)

Blain, A. W., Smail, I., Ivison, R. J., Kneib, J.-P., & Frayer, D. T. 2002, PhR, 369, 111
Borys, C., Chapman, S., Helpern, M., & Scott, D. 2003, MNRAS, 344, 385
Bourne, N., Dunlop, J. S., Merlin, E., et al. 2017, MNRAS, 467, 1360
Bouwens, R. J., Illingworth, G. D., Oesch, P. A., et al. 2015, ApJ, 803, 34
Bouwens, R. J., Oesch, P. A., Illingworth, G. D., Ellis, R. S., & Stefanon, M. 2017, ApJ, 843, 129
Carniani, S., Maiolino, R., De Zotti, G., et al. 2015, A&A, 584, 78
Casey, C. M., Chen, C.-C., Cowie, L. L., et al. 2013, MNRAS, 436, 1919
Casey, C. M., Cooray, A., Capak, P., et al. 2015, ApJL, 808, L33
Casey, C. M., Narayanan, D., & Cooray, A. 2014, PhR, 541, 45
Chapin, E. L., Berry, D. S., Gibb, A. G., et al. 2013, MNRAS, 430, 2545
Chapin, E. L., Pope, A., Douglas, S., et al. 2009, MNRAS, 398, 1793
Chapman, S. C., Blain, A. W., Ivison, R. J., & Smail, I. R. 2003a, Natur, 422, 695
Chapman, S. C., Blain, A. W., Smail, I., & Ivison, R. J. 2005, ApJ, 622, 772
Chapman, S. C., Windhorst, R., Odewahn, S., Yan, H., & Conselice, C. 2003b, ApJ, 599, 92
Chen, C.-C., Cowie, L. L., Barger, A. J., et al. 2013a, ApJ, 762, 81
Chen, C.-C., Cowie, L. L., Barger, A. J., et al. 2013b, ApJ, 776, 131
Chen, C.-C., Cowie, L. L., Barger, A. J., Wang, W.-H., & Williams, J. P. 2014, ApJ, 789, 12
Chen, C.-C., Smail, I., Ivison, R. J., et al. 2016, ApJ, 820, 82
Chen, C.-C., Smail, I., Swinbank, A. M., et al. 2015, ApJ, 799, 194
Chu, J. K., Sanders, D. B., Larson, K. L., et al. 2017, ApJS, 229, 25
Clements, D. L., Rigby, E., Maddox, S., et al. 2010, A&A, 518, L8
Condon, J. J. 1974, ApJ, 188, 279
Conselice, C. J., Chapman, S. C., & Windhorst, R. A. 2003, ApJL, 596, L5
Coppin, K., Chapin, E. L., Mortier, A. M. J., et al. 2006, MNRAS, 372, 1621
Cowie, L. L., Barger, A. J., Hsu, L.-Y., et al. 2017, ApJ, 837, 139
Cowie, L. L., Barger, A. J., & Kneib, J.-P. 2002, AJ, 123, 2197
Cowley, W. I., Lacey, C. G., Baugh, C. M., & Cole, S. 2015, MNRAS, 446, 1784
Danielson, A. L. R., Swinbank, A. M., Smail, I., et al. 2017, ApJ, 840, 78
Dannerbauer, H., Walter, F., & Morrison, G. E. 2008, ApJL, 673, L127
Dempsey, J. T., Friberg, P., Jenness, T., et al. 2013, MNRAS, 430, 2534
Dempsey, J. T., Holland, W. S., Chrysostomou, A., et al. 2012, Proc. SPIE, 8452, 2
Dunlop, J. S., McLure, R. J., Biggs, A. D., et al. 2017, MNRAS, 466, 861
Eales, S., Lilly, S., Gear, W., et al. 1999, ApJ, 515, 518
Fixsen, D. J., Dwek, E., Mather, J. C., Bennett, C. L., & Shafer, R. A. 1998, ApJ, 508, 123
Fujimoto, S., Ouchi, M., Ono, Y., et al. 2016, ApJS, 222, 1
Furusawa, H., Kosugi, G., Akiyama, M., et al. 2008, ApJS, 176, 1
Geach, J. E., Chapin, E. L., Coppin, K. E. K., et al. 2013, MNRAS, 432, 53
Geach, J. E., Dunlop, J. S., Halpern, M., et al. 2017, MNRAS, 465, 1789
Gispert, R., Lagache, G., & Puget, J. L. 2000, A&A, 360, 1
Glenn, J., Conley, A., Béthermin, M., et al. 2010, MNRAS, 409, 109
Greve, T. R., Ivison, R. J., Bertoldi, F., et al. 2004, MNRAS, 354, 779
Grogin, N., Kocevski, D., Faber, S. M., et al. 2011, ApJS, 197, 35
Hatsukade, B., Kohno, K., Aretxaga, I., et al. 2011, MNRAS, 411, 102
Hatsukade, B., Kohno, K., Umehata, H., et al. 2016, PASJ, 68, 36
Hatsukade, B., Ohta, K., Seko, A., Yabe, K., & Akiyama, M. 2013, ApJL, 769, L27
Hayward, C. C., Jonsson, P., Kereš, D., et al. 2012, MNRAS, 424, 951
Hayward, C. C., Kereš, D., Jonsson, P., et al. 2011, ApJ, 743, 159
Hayward, C. C., Narayanan, D., Kereš, D., et al. 2013, MNRAS, 428, 2529
Hodge, J. A., Karim, A., Smail, I., et al. 2013, ApJ, 768, 91
Hodge, J. A., Swinbank, A. M., Simpson, J. M., et al. 2016, ApJ, 833, 103
Högbom, J. A. 1974, A&AS, 15, 417
Holland, W. S., Bintley, D., Chapin, E. L., et al. 1999, MNRAS, 430, 2513
Holland, W. S., Robson, E. I., Gear, W. K., et al. 1999, MNRAS, 303, 659
Hsu, L.-Y., Cowie, L. L., Chen, C.-C., Barger, A. J., & Wang, W.-H. 2016, ApJ, 829, 25
Hughes, D. H., Serjeant, S., Dunlop, J., et al. 1998, Natur, 394, 241
Hung, C.-L., Caser, C. M., Chinag, Y.-K., et al. 2016, ApJ, 826, 130
Ivison, R. J., Lewis, A. J. R., Weiß, A., et al. 2016, ApJ, 832, 78

Jenness, T., Berry, D., Chapin, E., et al. 2011, in ASP Conf. Ser. 442, Astronomical Data Analysis Software and Systems XX, ed. I. N. Evans et al. (San Francisco, CA: ASP), 281
Jenness, T., Cavanagh, B., Economou, F., & Berry, D. S. 2008, in ASP Conf. Ser. 394, Astronomical Data Analysis Software and Systems XVII, ed. R. W. Argyle, P. S. Bunclark, & J. R. Lewis (San Francisco, CA: ASP), 565
Johansson, D., Sigurdarson, H., & Horellou, C. 2011, A&A, 527, 117
Karim, A., Swinbank, A. M., Hodge, J. A., et al. 2013, MNRAS, 432, 2
Knudsen, K. K., van der Werf, P. P., & Kneib, J.-P. 2008, MNRAS, 384, 1611
Koekemoer, A. M., Faber, S., Ferguson, H., et al. 2011, ApJS, 197, 36
Lacey, C. G., Baugh, C. M., Carlos, S. F., et al. 2016, MNRAS, 462, 3854
Laird, E. S., Nandra, K., Pope, A., & Douglas, S. 2010, MNRAS, 401, 2763
Maloney, P. R., Glenn, J., Aguirre, J. E., et al. 2005, ApJ, 635, 1044
Menéndez-Delmestre, K., Blain, A. W., Smail, I., et al. 2009, ApJ, 699, 667
Michałowski, M., Dunlop, J. S., & Koprowski, M. P. 2017, MNRAS, 469, 492
Michałowski, M., Hjorth, J., & Watson, D. 2010, A&A, 514, 67
Narayanan, D., Hayward, C. C., Cox, T. J., et al. 2010, MNRAS, 401, 1613
Narayanan, D., Turk, M., Feldmann, R., et al. 2015, Natur, 525, 496
Oliver, S. J., Wang, L., Smith, A. J., et al. 2010, A&A, 518, L21
Ono, Y., Ouchi, M., Kurono, Y., & Momose, R. 2014, ApJ, 795, 5
Oteo, I., Zwaan, M. A., Ivison, R. J., Smail, I., & Biggs, A. D. 2016, ApJ, 822, 36
Patanchon, G., Ade, P. R., Bock, J. J., et al. 2009, ApJ, 707, 1750
Pope, A., Chary, R.-R., Alexander, D. M., et al. 2008, ApJ, 675, 1171
Puget, J.-L., Abergel, A., Bernard, J.-P., et al. 1996, A&A, 308, L5
Reddy, N. A., & Steidel, C. C. 2009, ApJ, 692, 778
Roseboom, I. G., Dunlop, J. S., Cirasuolo, M., et al. 2013, MNRAS, 436, 430
Sawicki, M., & Thompson, D. 2006, ApJ, 642, 653
Scott, K. S., Yun, M. S., Wilson, G. W., et al. 2010, MNRAS, 405, 2260
Scoville, N., Aussel, H., Brusa, M., et al. 2007, ApJS, 172, 1
Serjeant, S., Dunlop, J. S., Mann, R. G., et al. 2003, MNRAS, 344, 887
Shu, X. W., Elbaz, E., Bourne, N., et al. 2016, ApJS, 222, 4
Simpson, J. M., Smail, I., Swinbank, A. M., et al. 2015a, ApJ, 799, 81
Simpson, J. M., Smail, I., Swinbank, A. M., et al. 2015b, ApJ, 807, 128
Simpson, J. M., Smail, I., Wang, W.-H., et al. 2017, ApJL, 884, L10
Simpson, J. M., Swinbank, A. M., Smail, I., et al. 2014, ApJ, 788, 125
Smail, I., Ivison, R. J., & Blain, A. W. 1997, ApJL, 490, L5
Smail, I., Ivison, R. J., Blain, A. W., & Kneib, J.-P. 2002, MNRAS, 331, 495
Smolčić, V., Novak, M., Bondi, M., et al. 2017, A&A, in press (arXiv:1703.09713)
Steidel, C. C., Adelberger, K. L., Giavalisco, M., Dickinson, M., & Pettini, M. 1999, ApJ, 519, 1
Stetson, P. B. 1987, PASP, 99, 191
Strandet, M. L., Weiß, A., Vieira, J. D., et al. 2016, ApJ, 822, 80
Swinbank, A. M., Papadopoulos, P. P., Cox, P., et al. 2011, ApJ, 742, 11
Swinbank, A. M., Simpson, J. M., Smail, I., et al. 2014, MNRAS, 438, 1267
Swinbank, A. M., Smail, I., Chapman, S. C., et al. 2010, MNRAS, 405, 234
Umehata, H., Tamura, Y., Kohno, K., et al. 2015, ApJL, 815, L8
Valiante, E., Lutz, D., Sturm, E., et al. 2007, ApJ, 660, 1060
Valiante, E., Lutz, D., Sturm, E., Genzel, R., & Chapin, E. L. 2009, ApJ, 701, 1814
Valiante, E., Smith, M. W. L., Eales, S., et al. 2016, MNRAS, 462, 3146
Vernstrom, T., Scott, D., Wall, J. V., et al. 2014, MNRAS, 440, 2791
Wang, S. X., Brandt, W. N., Luo, B., et al. 2013, ApJ, 778, 179
Wang, T., Elbaz, D., Daddi, E., et al. 2016, ApJ, 828, 56
Wang, W.-H., Cowie, L. L., & Barger, A. J. 2004, ApJ, 613, 655
Wang, W.-H., Cowie, L. L., & Barger, A. J. 2006, ApJ, 647, 74
Wang, W.-H., Cowie, L. L., Barger, A. J., & Williams, J. P. 2011, ApJL, 726, L18
Wang, W.-H., Cowie, L. L., van Saders, J., Barger, A. J., & Williams, J. P. 2007, ApJL, 670, L89
Wang, W.-H., Kohno, K., Hatsukade, B., et al. 2016, ApJ, 833, 195
Wardlow, J. L., Smail, I., Coppin, K. E. K., et al. 2011, MNRAS, 415, 1479
Weiß, A., Kovács, A., Coppin, K., et al. 2009, ApJ, 707, 1201
Wilkinson, A., Omar, A., Chen, C.-C., et al. 2017, MNRAS, 464, 1380
Younger, J. D., Giovanni, F., Huang, J.-S., et al. 2007, ApJ, 671, 1531
Zavala, J. A., Aretxaga, I., Geach, J. E., et al. 2017, MNRAS, 464, 3369
Zavala, J. A., Aretxaga, I., & Hughes, D. H. 2014, MNRAS, 443, 2384